Energetically Consistent Eddy-Diffusivity Mass-Flux Convective Schemes: 2. Implementation and Evaluation in an Oceanic Context

Manolis Perrot, Florian Lemarié

JAMES | Journal of Advances in Modeling Earth Systems

RESEARCH ARTICLE
10.1029/2024MS004616

Energetically Consistent Eddy-Diffusivity Mass-Flux Convective Schemes: 2. Implementation and Evaluation in an Oceanic Context

M. Perrot[1] **and F. Lemarié**[1]

[1]University Grenoble Alpes, Inria, CNRS, Grenoble INP, LJK, Grenoble, France

Key Points:

- Assumptions underlying the derivation of Eddy-Diffusivity Mass Flux (EDMF) scheme are evaluated in the oceanic context using Large Eddy Simulations simulations
- A new closure for the turbulent transport of Turbulent Kinetic Energy (TKE) taking into account mass-flux transport of TKE is proposed
- The energetically consistent continuous formulation exposed in Part I is guiding the derivation of an energy-conserving discretization

Correspondence to:

M. Perrot,
manolis.perrot@univ-grenoble-alpes.fr

Citation:

Perrot, M., & Lemarié, F. (2025). Energetically consistent eddy-diffusivity mass-flux convective schemes: 2. Implementation and evaluation in an oceanic context. *Journal of Advances in Modeling Earth Systems*, *17*, e2024MS004616. https://doi.org/10.1029/2024MS004616

Received 1 AUG 2024
Accepted 13 JUN 2025

Author Contributions:

Conceptualization: M. Perrot, F. Lemarié
Formal analysis: M. Perrot
Funding acquisition: F. Lemarié
Methodology: M. Perrot, F. Lemarié
Software: M. Perrot, F. Lemarié
Supervision: F. Lemarié
Validation: M. Perrot
Visualization: M. Perrot
Writing – original draft: M. Perrot
Writing – review & editing: F. Lemarié

Abstract A convective vertical mixing scheme rooted in the Eddy-Diffusivity Mass-Flux (EDMF) approach is carefully derived from first principles in Part I. In addition, consistent energy budgets between resolved and subgrid scales when using an EDMF scheme are presented for seawater and dry atmosphere. In this second part, we focus on oceanic convection with the following objectives: (a) justify in the oceanic context the assumptions made in Part I for the derivation of an EDMF scheme and a new Turbulent Kinetic Energy (TKE) turbulent transport term (b) show how continuous energy budgets can guide an energetically consistent discretization (c) quantify energy biases of inconsistent formulations, including double-counting errors due to inconsistent boundary conditions. The performance of the proposed energetically consistent EDMF scheme is evaluated against Large Eddy Simulations (LES) and observational data of oceanic convection. We systematically evaluate the sensitivity of numerical solutions to different aspects of the new formulation: energetic consistency, flux of TKE, flux of horizontal momentum and plume fractional area. Notably, when compared to LES data, energetic consistency is key to obtaining accurate TKE and turbulent transport of TKE profiles. To further illustrate that the EDMF concept is a credible alternative to the traditional approaches used in the oceanic context (using an enhanced vertical diffusion or a counter gradient term) the proposed scheme is validated in a single-column configuration against observational data of oceanic convection from the LION buoy.

Plain Language Summary In Earth system models, various important processes occur on scales that are too fine to be resolved with usual grid resolutions. Parameterizations have to be used to approximate the average effect of such processes on the scales resolved by a numerical model. The general objective of the proposed work is to approach the parameterization problem for boundary-layer turbulence in a "consistent" manner. Here the notion of consistency integrates various aspects: global energetic consistency, consistency with a particular averaging technique for the scale-separation, and the rigorous reduction of a physical system to a scale-aware parametric representation based on well-identified and justifiable approximations and hypotheses. In the first part of this work, we focused on theoretical aspects at the continuous level. We considered energy budgets including subgrid and resolved energies allowing for the proper coupling between the parameterization and the resolved dynamics. In this second part, we look at practical aspects of implementation as well as sensitivity to various choices in the scheme. This includes numerical discretization preserving energetic consistency, boundary conditions and their impact on energy conservation, plume area, turbulent kinetic energy transport and momentum flux parameterization. This research paves the way toward an alternative methodology to parameterize oceanic convection across scales.

1. Introduction

1.1. Context and Organization of the Paper

Oceanic vertical mixing parameterizations based on the Eddy-Diffusivity Mass-Flux (EDMF) concept have seen a growing interest in the past years (Garanaik et al., 2024; Giordani et al., 2020; Ramadhan et al., 2020). In the companion paper Perrot et al. (2025) (hereafter Part I), we provide a self-contained derivation from first principles of a convective mixing EDMF scheme. This type of closure involves separating vertical turbulent fluxes into two components: an eddy-diffusivity (ED) term that addresses local small-scale mixing in a near isotropic environment, and a mass-flux (MF) transport term that accounts for the non-local transport performed by vertically coherent plumes surrounded by the environment. Using the multi-fluid averaging underlying the MF concept, we review consistent energy budgets between resolved and subgrid scales for seawater and dry atmosphere, in

anelastic and Boussinesq settings. We show that when using an EDMF scheme, closed energy budgets can be recovered if: (a) bulk production terms of turbulent kinetic energy (TKE) by shear, buoyancy and transport include MF contributions; (b) boundary conditions are consistent with EDMF, to avoid spurious energy fluxes at the boundary. Moreover we show that lateral mixing between plumes and environment (referred as entrainment or detrainment) induces a net production of TKE via the shear term, and such production is enhanced when the horizontal drag coefficient is increased. Throughout the theoretical development of the scheme, we maintain transparency regarding underlying assumptions.

In this second part, we use LES of oceanic convection to: (a) evaluate the assumptions used in the derivation of the scheme using a conditional sampling of convective plumes, (b) propose a new formulation for TKE transport and (c) assess the sensitivity of the EDMF scheme to energetic consistency, transport of TKE, horizontal momentum transport and small plume area assumption. Additionally, we compare the scheme to the classical TKE + EVD mixing scheme used for oceanic deep-convection (TKE and Enhanced Vertical Diffusivity, Madec et al., 2019). We show how energy budgets derived in Part I can guide a consistent discretization of the TKE equation; and we quantify energy biases of potentially inconsistent formulations, including double-counting errors due to inconsistent boundary conditions.

The paper is organized as follows. In Section 2 we derive a new closure for the turbulent transport of TKE. In Section 3 we describe the two idealized LES test cases and assess the validity of hypotheses used in the derivation of the MF scheme. In Section 4 we derive a discretization that preserves the energetically consistent nature of EDMF equations. In Section 5 we evaluate the SCM against LES and realistic data, assess the impact of different parameterization aspects, and quantify energy biases of inconsistent formulations, including double-counting errors due to inconsistent boundary conditions.

1.2. Recap of Equations and Assumptions of Part I

We consider a Single Column Model (SCM) of the ocean in Boussinesq approximation (e.g., Tailleux & Dubos, 2024),

$$\begin{cases} \partial_t \overline{\boldsymbol{u}}_h = -\partial_z \overline{w' \boldsymbol{u}_h'} \\ \partial_t \overline{\theta} = -\partial_z \overline{w'\theta'} + \dfrac{\overline{\epsilon}}{c_p - \alpha g z} \\ \partial_t \overline{S} = -\partial_z \overline{w' S'} \end{cases} \tag{1}$$

where $\overline{\boldsymbol{u}}_h = (\overline{u}, \overline{v})$ is the horizontal velocity vector, $\overline{\theta}$ is conservative temperature, $\overline{S}$ is salinity, and $\overline{w'\boldsymbol{u}_h'}$, $\overline{w'\theta'}$, $\overline{w'S'}$ are the corresponding vertical turbulent fluxes, and we neglected the radiative heating term compared to Part I. Moreover $\overline{\epsilon}$ is the viscous dissipation of TKE, c_p is the seawater specific heat capacity and α is the thermal expansion coefficient. The notation $\overline{(\cdot)}$ indicates that the model's variables and fluxes are interpreted as *horizontal averages* over the numerical grid cell of their continuous counterpart. Thus, we have a simple and exact correspondence to compare SCM and LES data. Although viscous heating $\overline{\epsilon}/(c_p - \alpha g z)$ is usually neglected in the ocean (McDougall, 2003), we kept this term to work with properly closed energy budgets.

The EDMF parameterization relies on a decomposition of the horizontal grid area into an isotropic environment where turbulent flux is assumed diffusive, and an averaged plume (note that EDMF schemes with multiple plumes also exists, e.g. Han & Bretherton, 2019; Suselj et al., 2019). Then the flux of any variable $X = u, v, \theta, S$ is closed according to the decomposition

$$\overline{w'X'} = \underbrace{-K_X \partial_z \overline{X}}_{\text{ED}} + \underbrace{a_p w_p \left(X_p - \overline{X}\right)}_{\text{MF}} \tag{2}$$

where K_X is an eddy-diffusivity coefficient, a_p is the fractional area of the plume, w_p is the vertical velocity of the plume and X_p is the plume-related X quantity. In the present study, the eddy viscosities $K_u = K_v$ and diffusivities $K_\theta = K_S$ (that will be denoted K_ϕ in the remainder of the paper) in turbulent vertical fluxes are computed from a

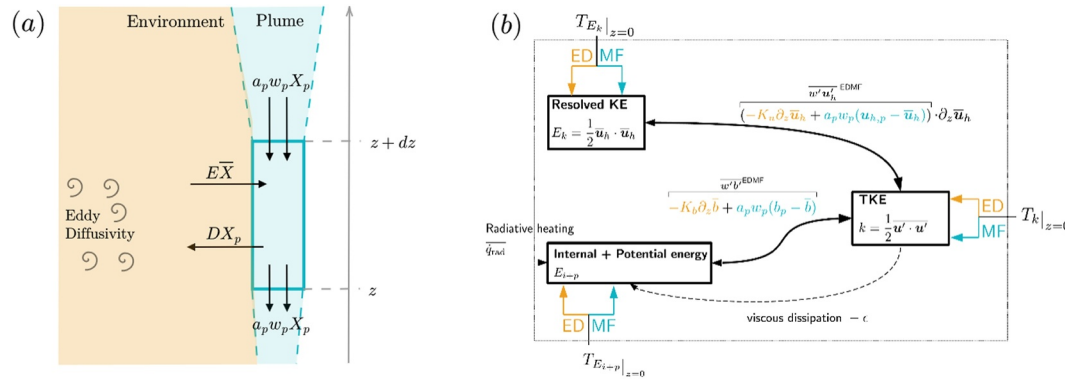

Figure 1. Schematic representation of panel (a) plume tracer budget, aside with eddy-diffusivity in the environment (b) energy budgets in Eddy-Diffusivity Mass Flux. For simplicity, plume sources terms $S_{X,p}$ have not been shown on panel (a).

turbulence closure model based on a prognostic equation for the TKE $k = \overline{\boldsymbol{u}' \cdot \boldsymbol{u}'}/2$ and a diagnostic computation of appropriate length scales (a.k.a. 1.5-order turbulence closure, see Appendix A).

Equations for plume-related quantities can be derived using a two-fluid averaging procedure of the original unaveraged equations. Standard EDMF formulations—followed in this study—rely on two main assumptions (see e.g. Part I or Yano, 2014): (a) stationarity of the plume, that is $\partial_t(a_p X_p) \ll \partial_z(a_p w_p X_p)$; (b) small-area occupied by the plume, that is considering $a_p \ll 1$ while keeping order one contribution of mass-flux $a_p w_p$ and source terms. Thus, the generic plume equation assumes a balance between vertical plume advection, horizontal entrainment (E) of environment fluid into the plume or detrainment (D) of plume fluid into the environment, and potential additional sources $S_{X,p}$ (see Figure 1a),

$$\partial_z(a_p w_p X_p) = E\overline{X} - DX_p + S_{X,p} \tag{3}$$

The comprehensive plume model equations with and without the assumption $a_p \ll 1$ are given in Table 1. A description of the closures are shown in Part I.

Total energy of the fluid in a Boussinesq approximation can be split into kinetic energy of the horizontal resolved flow $E_k = (\overline{\boldsymbol{u}}_h \cdot \overline{\boldsymbol{u}}_h)/2$ (usually referred as *mean* or *resolved kinetic energy*), residual turbulent (or subgrid) kinetic energy k, and $E_{i+p} = c_p\overline{\theta} - z\overline{b} + gz$, the sum of averaged internal energy and potential energy, where b is the buoyancy acceleration (see Tailleux & Dubos, 2024 and Part I). We were able to derive closed energy budgets, including the TKE equation in Part I (see Figure 1b).

$$\begin{cases} \partial_t E_k + \partial_z T_{E_k} &= -K_u\left(\partial_z \overline{\boldsymbol{u}}_h\right)^2 + a_p w_p (\boldsymbol{u}_{h,p} - \overline{\boldsymbol{u}}_h) \cdot \partial_z \overline{\boldsymbol{u}}_h \\ \partial_t k + \partial_z T_k &= -K_\phi \partial_z \overline{b} + a_p w_p \left(b_p - \overline{b}\right) + K_u\left(\partial_z \overline{\boldsymbol{u}}_h\right)^2 - a_p w_p (\boldsymbol{u}_{h,p} - \overline{\boldsymbol{u}}_h) \cdot \partial_z \overline{\boldsymbol{u}}_h - \overline{\epsilon} \\ \partial_t E_{i+p} + \partial_z T_{E_{i+p}} &= -\left(-K_\phi \partial_z \overline{b} + a_p w_p \left(b_p - \overline{b}\right)\right) + \overline{\epsilon} \end{cases} \tag{4}$$

where

$$T_{E_k} = \left(-K_u \partial_z \overline{\boldsymbol{u}}_h + a_p w_p (\boldsymbol{u}_{h,p} - \overline{\boldsymbol{u}}_h)\right) \cdot \overline{\boldsymbol{u}}_h \tag{5}$$

$$T_{E_{i+p}} = c_p\left(-K_\phi \partial_z \overline{\theta} + a_p w_p \left(\theta_p - \overline{\theta}\right)\right) - z\left(-K_\phi \partial_z \overline{b} + a_p w_p \left(b_p - \overline{b}\right)\right) \tag{6}$$

Based on conditional sampling of convective plumes, we propose a new formulation for the transport of TKE, T_k, in Section 2. A summary of plume and TKE equations, with and without the assumption $a_p \ll 1$ is also presented in Table 1.

Table 1
Summary of the Plume Equations Without the Small Plume Area Assumption, That is Without Assuming $a_p \ll 1$

$\sigma = \frac{1}{1-a_p}$	Rescaling coefficient
$X_e = \frac{1}{1-a_p}(\overline{X} - a_p X_p)$	Environmental variable, $X = \theta, S, \boldsymbol{u}_h$
$\overline{w'\theta'} = \sigma a_p w_p(\theta_p - \overline{\theta}) - K_\phi \partial_z \theta_e$	Vertical turbulent flux of temperature
$\overline{w'S'} = \sigma a_p w_p(S_p - \overline{S}) - K_\phi \partial_z S_e$	Vertical turbulent flux of salinity
$\overline{w'\boldsymbol{u}_h'} = \sigma a_p w_p(\boldsymbol{u}_{h,p} - \overline{\boldsymbol{u}}_h) - K_u \partial_z \overline{\boldsymbol{u}}_{h,e}$	Vertical turbulent momentum flux
$\partial_z(a_p w_p) = E - D$	Plume area conservation equation
$a_p w_p \partial_z \theta_p = \sigma E(\overline{\theta} - \theta_p) + \frac{a_p \epsilon_p}{c_p - \alpha g z}$	Plume temperature equation
$a_p w_p \partial_z S_p = \sigma E(\overline{S} - S_p)$	Plume salinity equation
$a_p w_p \partial_z \boldsymbol{u}_{h,p} = \sigma E(\overline{\boldsymbol{u}}_h - \boldsymbol{u}_{h,p}) + a_p w_p C_u \partial_z \overline{\boldsymbol{u}}_h$	Plume horizontal momentum equation
$a_p w_p \partial_z w_p = -\sigma b E w_p + a_p\left[aB_p + \sigma \frac{b'}{h}(w_p)^2\right]$	Plume vertical velocity equation
$B_p = b_{\text{eos}}(\theta_p, S_p) - b_{\text{eos}}(\overline{\theta}, \overline{S})$	Buoyancy forcing term
$a_p w_p \partial_z k_p = \sigma E\left((k - k_p) + \frac{1}{2}\|\boldsymbol{u}_p - \boldsymbol{u}\|^2\right) - a_p \epsilon_p$	Plume related TKE
$E = a_p C_{\text{ent}} \max(0, \partial_z w_p)$	Lateral entrainment closure
$D = -a_p C_{\text{det}} \min(0, \partial_z w_p) - a_p w_p \delta_0 \frac{1}{h}$	Lateral detrainment closure
$\partial_t k - \partial_z(K_k \partial_z k) = K_u(\partial_z \overline{\boldsymbol{u}}_{h,e})^2 - K_\phi \partial_z b_e$	ED related TKE production terms
$- \sigma a_p w_p((\boldsymbol{u}_{h,p} - \overline{\boldsymbol{u}}_h) \cdot \partial_z \overline{\boldsymbol{u}}_h - (b_p - \overline{b}))$	MF related TKE production terms
$- \partial_z\left(\sigma a_p w_p\left[k_p - k + \frac{1}{2}\|\boldsymbol{u}_p - \boldsymbol{u}\|^2\right]\right)$	MF related TKE transport term
$- \overline{\epsilon}$	TKE dissipation

Note. The small area limit is recovered if $\sigma \to 1$ and $X_e \to \overline{X}$. Details on closures are given in Perrot et al. (2025).

2. A New Closure for the Transport of TKE

The redistribution terms of TKE are often little discussed in turbulence parameterization since they do not contribute directly to the vertically integrated energy budgets. However, they are of great importance in convective conditions where non-local transport dominates (Witek et al., 2011). For instance, TKE produced close to the surface due to destabilizing buoyancy fluxes is then transported by coherent plumes into the mixed layer. Taking into account MF transport of TKE is thus essential to achieve local energetic consistency, and model TKE accurately at any level z.

Turbulent fluxes of TKE arise from the contribution of a TKE transport term, a pressure redistribution term, and a viscous flux (Mellor, 1973),

$$T_k = \frac{1}{2}\overline{w'\boldsymbol{u}' \cdot \boldsymbol{u}'} + \frac{1}{\rho_0}\overline{w'p'} - \nu \partial_z k \tag{7}$$

For oceanic flows, the viscous flux is negligibly small and will be omitted. We will assume that the pressure redistribution term can be incorporated into the transport term of TKE assuming proportionality, as it is usually done in convective boundary layer (CBL) schemes (e.g., Mellor, 1973). In numerical models, TKE transport is usually parameterized via K-diffusion, namely

$$\partial_z\left(\overline{w'\frac{\boldsymbol{u}' \cdot \boldsymbol{u}'}{2}}\right) \simeq -\partial_z(K_k \partial_z k) \tag{8}$$

where K_k is a diffusion coefficient associated to turbulent TKE transport. Alternatively, to derive a mass-flux based closure we can apply the plume/environment decomposition of the horizontal average to get the exact relation

$$\overline{w'\frac{\boldsymbol{u}'\cdot\boldsymbol{u}'}{2}} = \sum_{i=e,p} \underbrace{a_i\frac{1}{2}\overline{\boldsymbol{u}_i'\cdot\boldsymbol{u}_i'w_i'}}_{\mathrm{I}_i} + \underbrace{a_i(\boldsymbol{u}_i-\overline{\boldsymbol{u}})\cdot\overline{\boldsymbol{u}_i'w_i'}}_{\mathrm{II}_i} + \underbrace{a_i(w_i-\overline{w})\frac{1}{2}\overline{\boldsymbol{u}_i'\cdot\boldsymbol{u}_i'}}_{\mathrm{III}_i} + \underbrace{a_i\frac{1}{2}\|\boldsymbol{u}_i-\overline{\boldsymbol{u}}\|^2(w_i-\overline{w})}_{\mathrm{IV}_i} \tag{9}$$

where the subscript e denotes variables of the environment, and the subdomain moments are defined as

$$\overline{w_i'u_i'} = \frac{1}{A_i}\int_{A_i}(w-w_i)(u-u_i)\,\mathrm{d}x\,\mathrm{d}y \tag{10}$$

where A_i $(i = e,p)$ is the area occupied by the environment or the plume. Terms of Equation 9 are interpreted as follow: I_i is an intra-subdomain turbulent TKE transport; II_i can be interpreted as (horizontal and vertical) transport of Reynolds stress by the (horizontal and vertical) coherent velocities; III_i is transport of subdomain TKE by the coherent velocities (i.e., transport of TKE by mass-flux); IV_i is transport of convective kinetic energy by coherent velocities. Based on LES simulations (see Section 3.3), we found that: (a) I_p can be neglected, consistently with the small area limit; (b) II_e and II_p are almost compensating, thus the sum $\mathrm{II}_e + \mathrm{II}_p$ can be neglected. We can conveniently reformulate the remaining terms, except I_e, as (see Appendix B for details):

$$\mathrm{III}_e + \mathrm{III}_p + \mathrm{IV}_e + \mathrm{IV}_p = a_pw_p\frac{1}{1-a_p}\left(k_p + \frac{1}{2}\|\boldsymbol{u}_p-\overline{\boldsymbol{u}}\|^2 - k\right) \tag{11}$$

where subdomain TKEs are $k_i \coloneqq 1/2\overline{\boldsymbol{u}_i'\cdot\boldsymbol{u}_i'}$ $(i = e,p)$ and TKE can be decomposed as the sum of domain-averaged TKEs and subdomain TKEs:

$$k = \frac{1}{2}a_e\|\boldsymbol{u}_e-\overline{\boldsymbol{u}}\|^2 + a_ek_e + \frac{1}{2}a_p\|\boldsymbol{u}_p-\overline{\boldsymbol{u}}\|^2 + a_pk_p \tag{12}$$

In EDMF closures, turbulence is assumed isotropic in the environment, thus we close $I_e = \frac{1}{2}\overline{\boldsymbol{u}_e'\cdot\boldsymbol{u}_e'w_e'}$ with K-diffusion, similar to the standard practice for TKE-only schemes. Then assuming $\frac{1}{1-a_p}\simeq 1$ (i.e., the small area limit) we have

$$\overline{w'\frac{\boldsymbol{u}'\cdot\boldsymbol{u}'}{2}} = \underbrace{-K_k\partial_zk}_{\mathrm{ED}} + \underbrace{\overbrace{a_pw_p(k_p-k)}^{\text{Han \& Bretherton 2019}} + \overbrace{\frac{1}{2}a_pw_p^3}^{\text{Witek et al. 2011}} + \frac{a_pw_p}{2}\|\boldsymbol{u}_{h,p}-\overline{\boldsymbol{u}}_h\|^2}_{\text{new EDMF}} \tag{13}$$

It is interesting to note that we can recover existing formulations from the proposed closure (Equation 13): if $a_pw_p = 0$ it boils down to the classical eddy-diffusivity closure; if $k_p = k$ and $\boldsymbol{u}_{h,p} = \overline{\boldsymbol{u}}_h$ the term $1/2w_p^3$ proposed by Witek et al. (2011) is recovered; if TKE is treated as a tracer transported by the plume, then the formulation proposed by Han and Bretherton (2019) is recovered. However, we should mention that this latter treatment seems incorrect because the flux $\overline{w'\boldsymbol{u}'\cdot\boldsymbol{u}'/2}$ is not a second-order moment, but a third-order moment which involves additional terms when applying the plume/environment decomposition (see Equation 9).

Finally, one still needs to provide a value for k_p. Retaining vertical advection, entrainment, detrainment and dissipation terms of the k_p budget, and using the small area assumption, we have (see Appendix C for a detailed derivation).

$$a_pw_p\partial_zk_p = E\left(k-k_p+\frac{1}{2}\|\boldsymbol{u}_p-\overline{\boldsymbol{u}}\|^2\right) - a_p\epsilon_p \tag{14}$$

Table 2
Idealized Cases Parameters

Case	Q_0 (W m^{-2})	$(u^a_*)^2$ (m^2 s^{-2})	N_0^2 (s^{-2})	t_f (hr)	Fr_*
FC500	−500	0	1.962×10^{-6}	72	0
W005_C500	−500	0.05	1.962×10^{-6}	72	0.56

where the closure for dissipation is taken as $\epsilon_p = c_\epsilon / l_\epsilon (k_p)^{3/2}$ (c_ϵ is a constant and l_ϵ is a length scale, see Appendix A). Note that this equation differs from the one proposed by Han and Bretherton (2019). First, we retained dissipation. Second, the term $E\frac{1}{2}\|\boldsymbol{u}_p - \overline{\boldsymbol{u}}\|^2$ naturally emerges in the derivation from first principles, and initially represents a production of subplume TKE k_p via entrainment of environment/plume TKE difference, $\|\boldsymbol{u}_e - \boldsymbol{u}_p\|^2$ (see Appendix C). This energy transfer is absent in the closure proposed by Han and Bretherton (2019), since they treat k as a passive tracer and ignore the rigorous TKE decomposition exposed in Equation 12. We will now use LES to evaluate EDMF assumptions and the new closure of TKE transport.

3. Test Cases Description and Validation of Formulation

In this section we describe the reference idealized cases that will be further used in the study; then we describe the LES model and the conditional sampling technique used to identify convective plumes; finally we evaluate EDMF assumptions and the new closure of TKE transport.

3.1. Description of Idealized Cases

The two idealized cases considered are reminiscent of typical convective conditions in the ocean (e.g., Marshall & Schott, 1999), where convection into an initially resting ocean of constant stratification $\Delta\theta$ =1 K/1,000 m (corresponding N_0^2 =1.962 $\times 10^{-6}$ s^{-2}, according to the equation of state exposed in Section 3.2) is triggered by a surface cooling of Q_0 =−500 W m^{-2} (corresponding to a surface buoyancy loss of $B_0 = -2.456 \times 10^{-7}$ m^2 s^{-3}). In both cases, salinity is kept uniform at $S = 32.6$ psu. The first case (FC500) consists of free convection, where no wind stress is applied. In the second idealized case (W005_C500) a uniform wind stress along the meridional direction, of magnitude $(u^a_*)^2$ =0.05 m^2 s^{-2}, is applied. A summary of the parameters for each case can be found in table 2. To characterize wind-shear effects, we introduce the Froude number (Haghshenas & Mellado, 2019)

$$Fr_* = \frac{u^o_*}{N_0 L_0} \tag{15}$$

where the oceanic friction velocity u^o_* is defined via $\rho_o (u^o_*)^2 = \rho_a (u^a_*)^2$ (ρ_o and ρ_a being respectively the oceanic and atmospheric surface density), and the length scale $L_0 = \left(B_0/N_0^3\right)^{1/2}$ can be interpreted as an Ozmidov scale $\left(\epsilon/N^3\right)^{1/2}$ (Garcia & Mellado, 2014) which is a measure of the smallest eddy size affected by a background stratification N^2 in a turbulent field characterized by a viscous dissipation rate ϵ. After t_f =72 hr of simulation leading to a mixed layer depth (MLD) h (defined as the depth at which the buoyancy flux is minimum) of several hundred meters, various non-dimensional numbers can be used to characterize the flow. Their values can be found in Table 3. The ratio of the MLD to the Obukhov length (Obukhov, 1971 and Zheng et al., 2021 in the oceanic context) h/L_{Ob}, where

$$L_{Ob} = \frac{(u^o_*)^3}{-B_0} \tag{16}$$

is an estimate of the depth at which the production of TKE by turbulent shear is of the same order of magnitude as the production of TKE by buoyancy fluxes. Noting $w_* = (-B_0 h)^{1/3}$ the convective velocity scale (Deardorff, 1970), the ratio can be reinterpreted as

Table 3
Idealized Cases Non-Dimensional Parameters After 72 hr of Simulation

Case	h/L_{Ob}	Ri_h	Ri_*
FC500	∞	∞	97
W05_C500	5.7	310	97

$$\frac{h}{L_{Ob}} = \left(\frac{w_*}{u_*^o}\right)^3 \tag{17}$$

The Richardson number at the mixed layer base,

$$Ri_h = \frac{N_0^2}{\left(\frac{u_*^o}{h}\right)^2} \tag{18}$$

measures the destabilization by surface shear stresses of a stably stratified water column. At $t_f = 72$ hr, the case W005_C500 can be described by $h/L_{Ob} \simeq 5.7$ and $Ri_h \simeq 310$, which corresponds to a regime of strong deepening of the MLD according to Legay et al. (2024). Finally, for free convection cases (no wind) a convective Richardson number can be build as

$$Ri_* = \frac{N_0^2}{(w_*/h)^2} = \frac{N_0^2 h^{4/3}}{(-B_0)^{2/3}} = Ri_h \left(\frac{L_{Ob}}{h}\right)^{2/3} \tag{19}$$

It can be interpreted as follows. The time evolution of the MLD can be accurately described by the scaling (Turner, 1979; Van Roekel et al., 2018)

$$h \propto h_{\text{enc}} \tag{20}$$

where the *encroachment* depth is $h_{\text{enc}}(t) := \sqrt{2\frac{(-B_0)}{N_0^2}t}$. Then the ratio of the entrainment velocity $w_e = \frac{d}{dt}h$ to the convective velocity $w_* = (-B_0 h)^{1/3}$ reads

$$\frac{w_e}{w_*} \propto Ri_*^{-1} \tag{21}$$

3.2. LES Model Description and Conditional Sampling

The LES data have been generated by the non-hydrostatic model Méso-NH (Lac et al., 2018), using the Ocean-LES version developed by Jean-Luc Redelsperger. It is solving an anelastic Lipps-Hemler system adapted to the ocean, along with the linearized equation of state

$$b = g\alpha(\theta - \theta_0) \tag{22}$$

where g =9.81 m s^{-2} is gravitational acceleration, α =1.9 $\times$ 10^{-4} K^{-1} is the thermal expansion coefficient, and the reference temperature is θ_0 =286.65 K. Reference density is set to ρ_0 =1,027 kg m^{-3} and the specific heat capacity of seawater is c_p =3,985 J K^{-1} kg^{-1}. The model uses a second-order Runge-Kutta time stepping and spatial discretization of advection operators is performed with a fourth-order centered scheme. Explicit subgrid scale closures are computed via a 3-D turbulence scheme based on a prognostic equation of the subgrid TKE using a mixing-length scale, computed from the volume of a grid cell (Cuxart et al., 2000). The domain size is 1,000 m on the vertical and 7.5 km $\times$ 7.5 km on the horizontal, where doubly periodic conditions are applied. A resolution of 10 m on the vertical and 15 m on the horizontal is used. Each configuration is run for 72 hr with a time-step of 10 s. To assess the quality of the simulations, we checked that the subgrid TKE was never exceeding 20% of the TKE explicitly resolved by the LES (Pope, 2004). Via analysis of the total TKE budget, we checked that a quasi-steady regime is reached after a few hours of simulation (e.g., Garcia & Mellado, 2014). Moreover, at the end of the simulations, the typical size of coherent structures, which can be quantified by the horizontal integral length scale in the bulk of the mixed layer, is of the order O(500 m) $\ll$ 7.5 km. This suggests that the horizontal domain is large enough to provide a satisfactory statistical sampling of turbulent structures.

To identify plumes, we use a velocity-based conditional sampling adapted from Pergaud et al. (2009), where the plume area is defined as

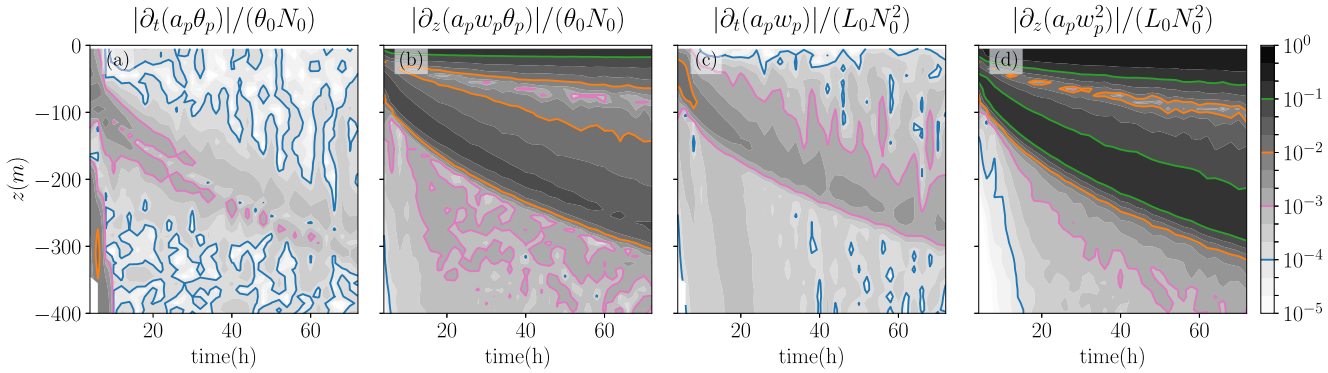

Figure 2. Temporal evolution of the normalized plume tendency $\partial_t(a_p X_p)$ and plume advection $\partial_z(a_p w_p X_p)$ terms ($X = \theta, w$), for the case FC500: (a) normalized temperature tendency, (b) normalized temperature advection, (c) normalized vertical velocity tendency, (d) normalized vertical velocity advection. Colored lines indicate thresholds to each power of ten.

$$A_p(z,t) = \left\{(x,y,z,t) \text{ such that } \overline{w}(z,t) - w(x,y,z,t) > m \times \max\left(\sqrt{\overline{w^{2'}}}(z,t), \sigma_{\min}(z,t)\right)\right\} \tag{23}$$

where the minimum standard deviation is chosen as $\sigma_{\min}(z,t) = 0.05/(-z)\int_z^0 \sqrt{\overline{w^{2'}}}(z',t)\,\mathrm{d}z'$. We do not use the tracer-based sampling of Couvreux et al. (2010) since it is valid only for small variations of the MLD. We neither utilize the "strong updraft" sampling of Siebesma et al. (2007) since it assumes that a_p is a given constant. However, we checked that similar conclusions could be drawn from such samplings. We used $m = 1$ similar to a number of previous studies (Couvreux et al., 2010; Greenhut & Khalsa, 1982; Park et al., 2016; Pergaud et al., 2009; Zhou et al., 2018). However, fractional area a_p exhibits a sensitivity for both velocity-based and tracer based samplings (e.g., Figure B2 of Zhou et al., 2018).

3.3. Evaluation of the Steady Plume and Small Area Hypotheses

In this section, we directly assess the validity of the primary assumptions underlying the EDMF scheme, namely that plumes are stationary and that their fractional area is negligible compared to the total grid area. Figures 2 and 3 demonstrate that the temporal tendency terms of the plume are approximately $O(10^{-1} - 10^{-2})$ smaller than the advective terms, in agreement with the scaling $1/(N_0 t)$ derived in Part I. This supports the use of the steady plume hypothesis. Figures 4 and 5 present vertical profiles of temperature, vertical velocity, plume fractional area, and temperature flux for the idealized cases FC500 and W005_C500. The fractional area of the plume, a_p, ranges between 10% and 20% of the total grid area, consistent with previous studies (e.g., Couvreux et al., 2010). While these values may be sensitive to the choice of the threshold m in the conditional sampling, they call into question the validity of the assumption that a_p is negligible. This motivates the analysis in Section 5.4,

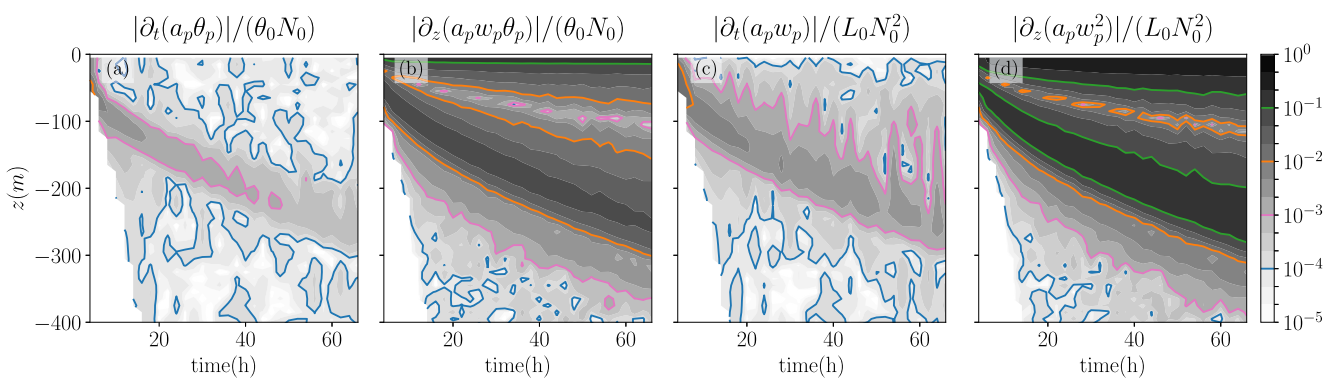

Figure 3. Same as Figure 2 for the case W005_C500.

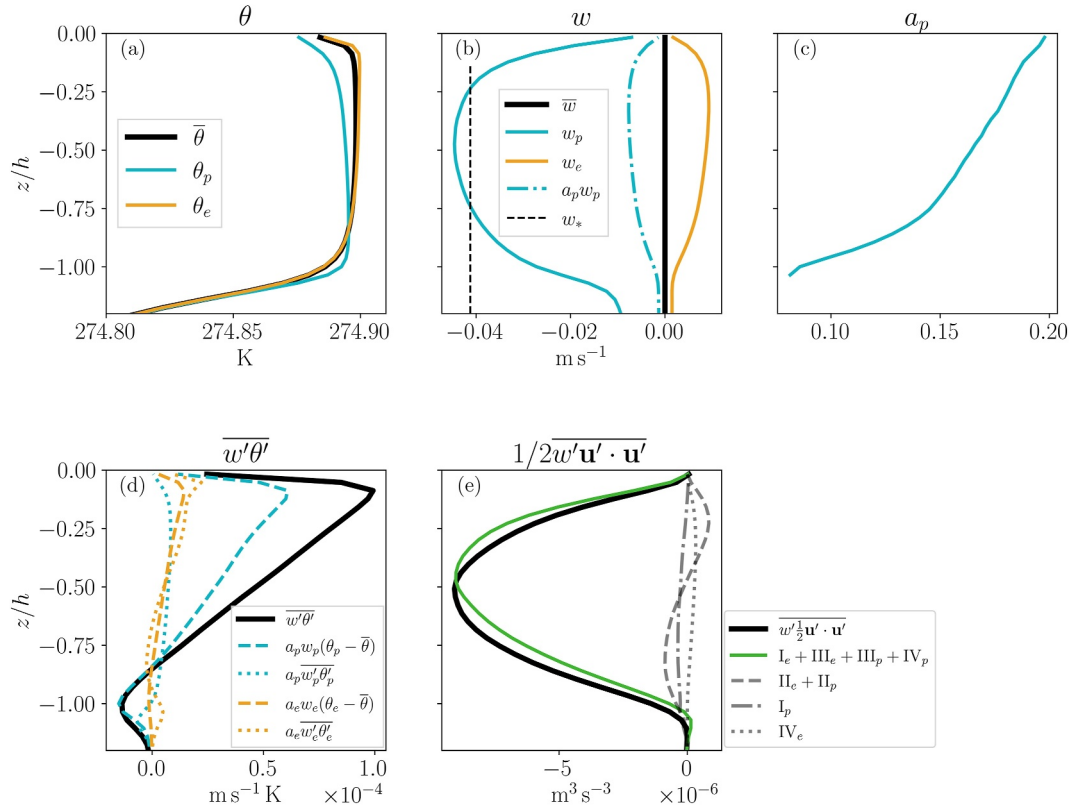

Figure 4. Large Eddy Simulations vertical profiles of panel (a) potential temperature, (b) vertical velocity, (c) plume fractional area, (d) temperature flux and (e) Turbulent Kinetic Energy flux for the FC500 case after 72 hr of simulation. For each field, the black line represents a horizontal average over the whole grid cell, the blue line represents an average over the plume area and the orange line represents an average over the environment area. In panel (b) the blue dotted line represents $a_p w_p$, and the gray dashed line represents the value of the free convective velocity scale w_*. In panel (d), total flux is in black, plume fluxes in blue (MF is dashed and subplume is dotted), and environment fluxes in orange (same line styles). In panel (e) are represented the total flux (black) and the contributions from the combined terms $I_e + III_e + III_p + IV_p$ (blue), $II_e + II_p$ (dashed gray), I_p (dash-dotted gray) and III_p (dotted gray) (see Section 2 for details).

where the constraint of a small a_p is relaxed. The convective velocity scale w_* is found to be a good predictor of the plume vertical velocity w_p magnitude (panel (b)). The contribution of the mass-flux term, $a_p w_p(\theta_p - \overline{\theta})$ (panel (d)), to the total temperature flux increases with depth, eventually reaching near-complete dominance in the entrainment layer. The approximate validity of the assumption $a_p w_p(\theta_p - \overline{\theta}) \gg a_p\overline{w'_p\theta'_p}, a_e w_e(\theta_e - \overline{\theta})$ aligns with the smallness of a_p. However, we observe that $a_p\overline{w'_p\theta'_p}$ and $a_e\overline{w'_e\theta'_e}$ are of comparable magnitude. This contrasts with conventional approaches, which typically assume that residual fluxes are primarily driven by turbulence in the environment alone (Perrot et al., 2025; Siebesma et al., 2007; Tan et al., 2018). As highlighted by Zhou et al. (2018), this finding suggests that further investigation is needed to evaluate the suitability of K-diffusion as a parameterization for these residual terms.

The plume/environment decomposition of the vertical transport of TKE $1/2\overline{w'\boldsymbol{u}'\cdot\boldsymbol{u}'}$ is presented in Figures 4e and 5e. The dominant terms exposed in Equation 11 explain well the total flux.

The idealized LES have allowed us to examine the validity of hypotheses used to derive the continuous formulation of our energetically consistent EDMF scheme. Now we turn to numerical discretization of such scheme.

4. Discretization of Energetically Consistent EDMF Equations

In this section, we derive a discretization that satisfies the conservative energy exchange described in Part I (see also the introduction in Section 1) at a discrete level when using EDMF. This is achieved through discrete mean kinetic, turbulent kinetic, and potential energy budgets. This type of approach has already been proposed by

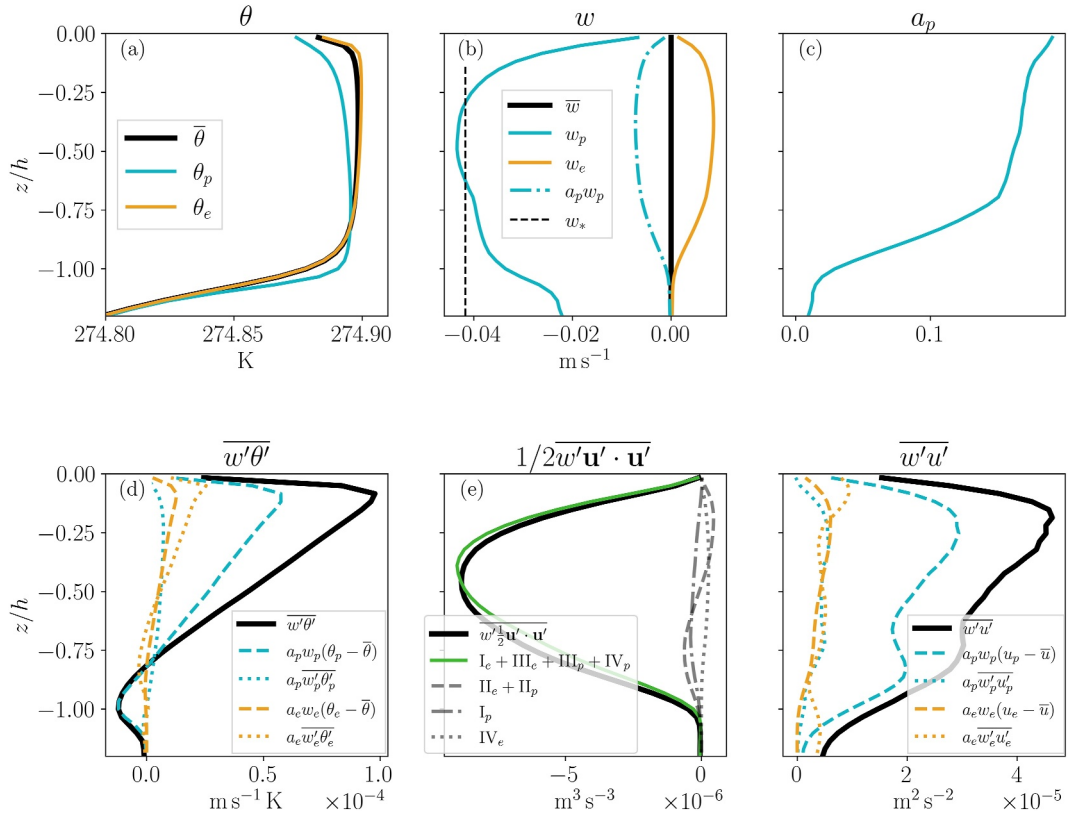

Figure 5. Same as Figure 4 for the case W005_C500 except for Panel (f): decomposition of the $\overline{w'u'}$ flux, total flux is in black, plume fluxes in blue (MF is dashed and subplume is dotted), and environment fluxes in orange (same line styles).

Burchard (2002) in the ED case to derive an energy-conserving discretization method for the shear and buoyancy production terms in TKE equation. In what follows, we generalize this approach to the EDMF case. This section is divided into 2 subsections, the first about the coupling between ED and MF schemes within the time-stepping algorithm and the second about an energy-conserving discretization of TKE production and destruction terms. For readers interested in a practical implementation of the proposed EDMF scheme in a numerical model, full details of a simple discretization of the MF equations are given in Appendix D including the way the MLD h is computed. The proposed discretization guarantees that w_p is strictly negative, that a_p is bounded between 0 and 1, and that the continuity and tracer equations are compatible, without the need for an iterative solution procedure.

4.1. Coupling ED and MF Schemes

In the EDMF approach, the following equation must be advanced in time (with $X = u, v, \theta, S$):

$$\partial_t \overline{X} = \partial_z\left(K_X \partial_z \overline{X}\right) - \partial_z\left(a_p w_p\left(X_p - \overline{X}\right)\right) \tag{24}$$

This amounts to coupling an ED scheme which provides K_X and a MF scheme which provides $a_p w_p$ and X_p. The numerical treatment of such coupling can be approached in 2 ways: either by integrating the 2 schemes sequentially or simultaneously. For the numerical experiments discussed in Section 5 we chose a *ED-then-MF* strategy corresponding to the following temporal integration for the single-column model (leaving aside the Coriolis and solar penetration terms, and for $\overline{\phi} = \overline{\theta}, \overline{S}$).

$$\underline{\text{ED step}}$$
$$\overline{\phi}^{n+1,\star} = \overline{\phi}^{n} + \Delta t \partial_z\left(K_\phi(k^n, b^n)\partial_z \overline{\phi}^{n+1,\star}\right) \tag{25}$$

$$\overline{\boldsymbol{u}}_h^{n+1,\star} = \overline{\boldsymbol{u}}_h^n + \Delta t \partial_z \left(K_{\boldsymbol{u}}(k^n, b^n) \partial_z \overline{\boldsymbol{u}}_h^{n+1,\star} \right) \tag{26}$$

$$\overline{b}^{n+1,\star} = b_{\text{eos}}\left(\overline{\phi}^{n+1,\star} \right) \tag{27}$$

MF step

$$\left[a_p, w_p, \phi_p, \boldsymbol{u}_{h,p}, B_p \right] = \text{MF}\left(\overline{\phi}^{n+1,\star}, \overline{b}^{n+1,\star}, \overline{\boldsymbol{u}}_h^{n+1,\star} \right) \tag{28}$$

$$\overline{\phi}^{n+1} = \overline{\phi}^{n+1,\star} - \Delta t \partial_z \left(a_p w_p \left(\phi_p - \overline{\phi}^{n+1,\star} \right) \right) \tag{29}$$

$$\overline{\boldsymbol{u}}_h^{n+1} = \overline{\boldsymbol{u}}_h^{n+1,\star} - \Delta t \partial_z \left(a_p w_p \left(\boldsymbol{u}_{h,p} - \overline{\boldsymbol{u}}_h^{n+1,\star} \right) \right) \tag{30}$$

TKE update

$$k^{n+1,\star} = k^n + \Delta t \partial_z \left(K_k(k^n, b^n) \partial_z k^{n+1,\star} \right) + \mathcal{F}_k \left(\overline{b}^{n+1,\star}, \overline{\boldsymbol{u}}_h^{n+1,\star}, \overline{\boldsymbol{u}}_h^n, a_p, w_p, \boldsymbol{u}_{h,p}, B_p \right) - \overline{\epsilon} \tag{31}$$

$$k_p = \text{MF}\left(k^{n+1,\star}, \overline{\boldsymbol{u}}_h^{n+1,\star}, \boldsymbol{u}_{h,p}, a_p \right) \tag{32}$$

$$k^{n+1} = k^{n+1,\star} - \Delta t \partial_z \left(a_p w_p \left(k_p - k^{n+1,\star} \right) \right) \tag{33}$$

where the MF(.) function represents the computation of mass-flux quantities as described in Appendix D and $\mathcal{F}_k$ in Equation 31 contains the TKE forcing terms (production/destruction by shear and buoyancy) as well as the vertical divergence of the last two terms of the TKE turbulent flux (13). As we will see later in this section, the energetically consistent discretization of the TKE production term by shear involves both $\overline{\boldsymbol{u}}_h^{n+1,\star}$ and $\overline{\boldsymbol{u}}_h^n$ (see Equation 53), which explains their presence in $\mathcal{F}_k$. The viscous dissipation we consider for numerical experiments is parameterized as $\overline{\epsilon} = \frac{c_\epsilon}{l_\epsilon} k^{3/2}$ (see Appendix A) where the $k^{3/2}$ term is discretized as $k^{n+1,\star}\sqrt{k^n}$. In oceanic models, the "ED step" is classically computed using an Euler backward (implicit) scheme. With the proposed approach, the MF scheme takes as input a state already updated by the ED scheme (and by the solar penetration and non-solar surface heat flux which are applied during the "ED step"), via a forward (explicit) scheme. The convection scheme therefore uses a state whose static stability is representative of the current time-step and external forcing. Ultimately, with the proposed approach, the various stages can be expressed directly as follows

$$\overline{\phi}^{n+1} = \overline{\phi}^n + \Delta t \partial_z \left(K_\phi \partial_z \overline{\phi}^{n+1,\star} - a_p w_p \left(\phi_p - \overline{\phi}^{n+1,\star} \right) \right) \tag{34}$$

$$\left[a_p, w_p, \phi_p \right] = \text{MF}\left(\overline{\phi}^{n+1,\star} \right) \tag{35}$$

which reflects the fact that the ED part and the MF part are properly synchronized in time, as they consider the same mean fields. In the case where stratification is stable throughout the column, the mass flux scheme returns a zero fraction a_p and we simply obtain $\overline{\phi}^{n+1} = \overline{\phi}^{n+1,\star}$.

On the other hand, the approach of simultaneously considering the ED and MF parts in a single tridiagonal problem (a.k.a. the *ED-and-MF* strategy, e.g. Giordani et al. (2020)) would lead to

$$\overline{\phi}^{n+1} = \overline{\phi}^n + \Delta t \partial_z \left(K_\phi \partial_z \overline{\phi}^{n+1} - a_p w_p \left(\phi_p - \overline{\phi}^{n+1} \right) \right) \tag{36}$$

$$\left[a_p, w_p, \phi_p \right] = \text{MF}\left(\overline{\phi}^n \right) \tag{37}$$

In this case, the mass flux variables are computed using mean fields at time n. Indeed, ϕ_p has been computed using $\overline{\phi}^n$ while it is applied at time $n + 1$.

To assess the numerical stability of the two strategies in the sense of Von Neumann analysis, the relevant dimensionless parameters are $\sigma_0 = E\Delta t, \sigma_1 = -a_p w_p \Delta t/\Delta z$, and $\sigma_2 = K_\phi \Delta t/\Delta z^2$. The *ED-and-MF* strategy is stable under the constraint $\sigma_0 \leq 2$ jointly with $0 \leq C_u \leq 1$. The same stability constraints apply to the *ED-then-MF* strategy, which has an additional constraint on σ_1 $\left((1 - C_u)\,\sigma_1 \leq \left(1 - \sigma_0 + \sqrt{1 + 8\sigma_2}\right)/2\right)$ due to the explicit-in-time treatment of the MF term in the mean flow equations. In the following, we focus on the sequential *ED-then-MF* strategy and now turn our attention to the spatial discretization of an energetically consistent EDMF scheme.

4.2. Energy Consistent Discretization of TKE Dissipation and Production Terms

We consider the standard grid arrangement used in oceanic models which are usually discretized on a Lorenz grid in the vertical (density is located at the center of the cells on the vertical). We consider N grid cells in the vertical with thickness $\Delta z_j = z_{j+1/2} - z_{j-1/2}$ ($z_{1/2} = -H$ and $z_{N+1/2} = 0$ the surface) such that $\sum_{j=1}^{N} \Delta z_j = -H$. Traditionally, turbulent quantities like turbulent kinetic energy k and eddy diffusivities K_X are naturally located on the interfaces at $z_{j+1/2}$ to avoid interpolations when computing the vertical gradients of the turbulent fluxes. For the discrete values, not to interfere with the grid indices, the subscript p for the plume quantities is now a superscript such that plume quantities are now noted $X^p_{j+1/2} = X_p(z = z_{j+1/2})$. In the following, we consider that the plume quantities and k are discretized at cell interfaces and the mean quantities are discretized at cell centers.

The turbulent flux $\overline{w'X'}$ (for $X = u, v, b, \theta$) is discretized at cell interfaces using a standard second-order scheme for the ED component and a first-order upwind scheme for the MF component. The discrete form $\mathcal{J}^X_{j+1/2}$ of turbulent fluxes considered is therefore ($1 \leq j \leq N - 1$):

$$\left(\overline{w'X'}\right)_{j+1/2} = \mathcal{J}^X_{j+1/2} = -K^X_{j+1/2}\frac{\left(\delta_z \overline{X}\right)^{n+1,\star}_{j+1/2}}{\Delta z_{j+1/2}} + \left(a^p w^p\right)_{j+1/2}\left(X^p_{j+1/2} - \overline{X}^{n+1,\star}_j\right) \tag{38}$$

with $\left(\delta_z \overline{X}\right)^{n+1,\star}_{j+1/2} = \overline{X}^{n+1,\star}_{j+1} - \overline{X}^{n+1,\star}_j$, $[a^p, w^p, X^p] = \mathrm{MF}\left(\overline{X}^{n+1,\star}\right)$ and $\Delta z_{j+1/2} = z_{j+1} - z_j$. Because of the upwind discretization of the MF term, the mean value at level j, $\overline{X}^{n+1,\star}_j$, is used on the second term of the right-hand side. Boundary conditions for the fluxes are given by,

$$\mathcal{J}^\theta_{1/2} = 0, \quad \mathcal{J}^S_{1/2} = 0, \quad \mathcal{J}^u_{1/2} = 0 \tag{39}$$

$$\mathcal{J}^\theta_{N+1/2} = \overline{w'\theta'}_0, \quad \mathcal{J}^S_{N+1/2} = \overline{w'S'}_0, \quad \mathcal{J}^u_{N+1/2} = -\frac{\tau_x}{\rho_0} \tag{40}$$

that is that total ED + MF numerical fluxes equal the physical fluxes. Remark that boundary conditions are more commonly imposed for ED and MF schemes separately. In such case, one should carefully check that the combination of boundary conditions on ED and MF terms results in a physical flux, to avoid double-counting errors (see Section 5.1; see also Section 2.4 of Perrot et al. (2025)).

4.2.1. Discrete Mean Kinetic Energy Equation

For simplicity, we consider for the rest of this section only the $\overline{u}$ velocity component; it is straightforward to perform the same derivation including $\overline{v}$. Multiplying the discrete equation for $\overline{u}_j$ by $\overline{u}^{n+1/2}_j = \left(\overline{u}^{n+1}_j + \overline{u}^n_j\right)/2$ we obtain

$$\frac{\left(\overline{u}^{n+1}_j\right)^2 - \left(\overline{u}^n_j\right)^2}{2\Delta t} = -\frac{\overline{u}^{n+1/2}_j}{\Delta z_j}\left[\mathcal{J}^u_{j+1/2} - \mathcal{J}^u_{j-1/2}\right] \tag{41}$$

After some simple algebra $\left(\text{i.e. multiplication of } \mathcal{J}^u_{j+1/2} \text{ by } \overline{u}^{n+1/2}_j = -\frac{1}{2}\left(\delta_z \overline{u}\right)^{n+1/2}_{j+1/2} + \overline{u}^{n+1/2}_{j+1/2} \text{ and of } \mathcal{J}^u_{j-1/2} \text{ by } \overline{u}^{n+1/2}_j = \frac{1}{2}\left(\delta_z \overline{u}\right)^{n+1/2}_{j-1/2} + \overline{u}^{n+1/2}_{j-1/2}\right)$ the mean kinetic energy equation can be expressed as

$$\frac{\left(\overline{u}_j^{n+1}\right)^2-\left(\overline{u}_j^{n}\right)^2}{2\Delta t}+\frac{1}{\Delta z_j}\left(\overline{u}_{j+1/2}^{n+1/2}\,\mathcal{J}_{j+1/2}^{u}-\overline{u}_{j-1/2}^{n+1/2}\,\mathcal{J}_{j-1/2}^{u}\right)=\frac{1}{2\Delta z_j}\left\{\left(\delta_z\overline{u}\right)_{j+1/2}^{n+1/2}\mathcal{J}_{j+1/2}^{u}+\left(\delta_z\overline{u}\right)_{j-1/2}^{n+1/2}\mathcal{J}_{j-1/2}^{u}\right\} \tag{42}$$

where the terms in curly brackets on the right-hand side contribute to the discrete expressions of the ED and MF TKE production terms by shear while the flux divergence term corresponds to the $\partial_z T_{E_k}$ term in Equation 4. In Equation 42, we considered $\overline{u}_{j+1/2}^{n+1/2}=\frac{1}{2}\left(\overline{u}_{j+1}^{n+1/2}+\overline{u}_{j}^{n+1/2}\right)$ and a similar definition for $\left(\delta_z\overline{u}\right)_{j+1/2}^{n+1/2}$. The vertically integrated discrete budget reads

$$\begin{aligned}&\sum_{j=1}^{N}\Delta z_j\left(\frac{\left(\overline{u}_j^{n+1}\right)^2-\left(\overline{u}_j^{n}\right)^2}{2\Delta t}\right)+\overbrace{\overline{u}_{N+1/2}^{n+1/2}\mathcal{J}_{N+1/2}^{u}-\overline{u}_{1/2}^{n+1/2}\mathcal{J}_{1/2}^{u}}^{\text{surf. \& bot. fluxes}}\\&=\frac{1}{2}\left(\left(\delta_z\overline{u}\right)_{N+1/2}^{n+1/2}\mathcal{J}_{N+1/2}^{u}+\left(\delta_z\overline{u}\right)_{1/2}^{n+1/2}\mathcal{J}_{1/2}^{u}\right)+\underbrace{\sum_{j=1}^{N-1}\left(\delta_z\overline{u}\right)_{j+1/2}^{n+1/2}\mathcal{J}_{j+1/2}^{u}}_{\text{mechanical prod. of TKE}}\end{aligned} \tag{43}$$

The second term on the left-hand side corresponds to the surface and bottom energy fluxes. Since $\overline{u}$ is defined at cell centers, choices have to be made for the values of $\overline{u}_{N+1/2}^{n+1/2}$ and $\overline{u}_{1/2}^{n+1/2}$ in order to compute surface a bottom energy fluxes. For numerical applications, we will use the simple assumption $\overline{u}_{N+1/2}^{n+1/2}=\overline{u}_{N}^{n+1/2}$, $\overline{u}_{1/2}^{n+1/2}=\overline{u}_{1}^{n+1/2}$ as in Burchard (2002). The second term on the right-hand side will correspond to (minus) the summed mechanical production of TKE. One might be tempted to also interpret the first term on the right-hand side as a transfer of KE to TKE by shear. However, since TKE is discretized on cell interfaces, this term cannot be included in the discrete TKE budget. In order to recover an analog of continuous energy budgets, we necessarily have to set $\left(\delta_z\overline{u}\right)_{N+1/2}^{n+1/2}=\left(\delta_z\overline{u}\right)_{1/2}^{n+1/2}=0$ as in Burchard (2002) (for models using TKE defined at cell centers, this term would have to be retained). Using the momentum flux boundary conditions (39), the vertically integrated discrete budget is thus simplified into

$$\sum_{j=1}^{N}\Delta z_j\left(\frac{\left(\overline{u}_j^{n+1}\right)^2-\left(\overline{u}_j^{n}\right)^2}{2\Delta t}\right)-\overline{u}_{N+1/2}^{n+1/2}\frac{\tau_x}{\rho_0}=\sum_{j=1}^{N-1}\left(\delta_z\overline{u}\right)_{j+1/2}^{n+1/2}\mathcal{J}_{j+1/2}^{u} \tag{44}$$

4.2.2. Discrete Mean Internal and Potential Energy Equation

We consider the energy $c_p\overline{\theta}-z\overline{b}$ which satisfies the discrete evolution equation

$$\frac{\left(c_p\overline{\theta}-z\overline{b}\right)_j^{n+1}-\left(c_p\overline{\theta}-z\overline{b}\right)_j^{n}}{\Delta t}=-\frac{c_p}{\Delta z_j}\left[\mathcal{J}_{j+1/2}^{\theta}-\mathcal{J}_{j-1/2}^{\theta}\right]+\frac{z_j}{\Delta z_j}\left[\mathcal{J}_{j+1/2}^{b}-\mathcal{J}_{j-1/2}^{b}\right]+\epsilon_j \tag{45}$$

where $\mathcal{J}_{j+1/2}^{b}=\alpha\mathcal{J}_{j+1/2}^{\theta}-\beta\mathcal{J}_{j+1/2}^{S}$, and β is the haline contraction coefficient. After some simple algebra (i.e., multiplication of $\mathcal{J}_{j+1/2}^{b}$ by $z_j=-\frac{1}{2}\Delta z_{j+1/2}+z_{j+1/2}$ and of $\mathcal{J}_{j-1/2}^{b}$ by $z_j=\frac{1}{2}\Delta z_{j-1/2}+z_{j-1/2}$), the discrete energy equation can be expressed as

$$\begin{aligned}&\frac{\left(c_p\overline{\theta}-z\overline{b}\right)_j^{n+1}-\left(c_p\overline{\theta}-z\overline{b}\right)_j^{n}}{\Delta t}+\frac{1}{\Delta z_j}\left[\left(c_p\,\mathcal{J}_{j+1/2}^{\theta}-z_{j+1/2}\,\mathcal{J}_{j+1/2}^{b}\right)-\left(c_p\,\mathcal{J}_{j-1/2}^{\theta}-z_{j-1/2}\,\mathcal{J}_{j-1/2}^{b}\right)\right]\\&=-\frac{1}{2\Delta z_j}\left\{\Delta z_{j+1/2}\,\mathcal{J}_{j+1/2}^{b}+\Delta z_{j-1/2}\,\mathcal{J}_{j-1/2}^{b}\right\}+\epsilon_j\end{aligned} \tag{46}$$

where the terms in curly brackets on the right-hand side contribute to the discrete expressions of the ED and MF TKE buoyancy production/destruction terms while the flux divergence term corresponds to the $\partial_z T_{E_{i+p}}$ term in Equation 4.

Summing over vertical levels and using the no-flux bottom boundary condition (Equation 39), the vertically integrated discrete budget reads

$$\sum_{j=1}^{N} \Delta z_j \left(\frac{\left(c_p \overline{\theta} - z\overline{b}\right)_j^{n+1} - \left(c_p \overline{\theta} - z\overline{b}\right)_j^{n}}{\Delta t} \right) + c_p \, \mathcal{J}^{\theta}_{N+1/2} + \frac{1}{2} \Delta z_{N+1/2} \, \mathcal{J}^{b}_{N+1/2} = -\sum_{j=1}^{N-1} \Delta z_{j+1/2} \, \mathcal{J}^{b}_{j+1/2} + \sum_{j=1}^{N} \Delta z_j \epsilon_j \tag{47}$$

4.2.3. Constraints for Discrete Energetic Consistency

In the same spirit as Burchard (2002), the discrete energy budgets (42) and (46) can be used to derive an a priori energy-conserving discretization of the shear (Sh) and buoyancy ($\mathcal{B}$) production terms for turbulent kinetic energy. The TKE variable is naturally located at cell interfaces in most ocean models. A discrete expression for its evolution equation is given by:

$$\frac{k^{n+1}_{j+1/2} - k^{n}_{j+1/2}}{\Delta t} = -\frac{1}{\Delta z_{j+1/2}} [\mathcal{G}_{j+1} - \mathcal{G}_j] + \mathrm{Sh}_{j+1/2} + \mathcal{B}_{j+1/2} - \epsilon_{j+1/2} \tag{48}$$

The turbulent transport of TKE consistent with Equation 13 is

$$\mathcal{G}_j = -K^k_j \frac{k^{n+1}_{j+1/2} - k^{n+1}_{j-1/2}}{\Delta z_j} + (a^p w^p)_{j+1/2} (k^p_{j+1/2} - k^n_{j-1/2}) + \frac{(a^p w^p)_{j+1/2}}{2} \left(\left(w^p_{j+1/2}\right)^2 + \left(u^p_{j+1/2} - \overline{u}^{n+1,\star}_j\right)^2 \right) \tag{49}$$

where a first-order upwind scheme is used to discretize the different components at cell centers. In Equation 49, K^k_j is obtained from $K^k_{j+1/2}$ and $K^k_{j-1/2}$ using a harmonic mean. No if-statement is necessary to determine the upwinding direction as we know a priori that the vertical velocity w^p associated with the plumes is negative. Using Equations 44 and 47, the constraints for energetic consistency between the mean and turbulent energies at the discrete level lead to

$$\sum_{j=1}^{N-1} \Delta z_{j+1/2} \mathrm{Sh}_{j+1/2} = -\sum_{j=1}^{N-1} \left(\delta_z \overline{u}\right)^{n+1/2}_{j+1/2} \mathcal{J}^{u}_{j+1/2} \tag{50}$$

$$\sum_{j=1}^{N-1} \Delta z_{j+1/2} \mathcal{B}_{j+1/2} = \sum_{j=1}^{N-1} \Delta z_{j+1/2} \, \mathcal{J}^{b}_{j+1/2} \tag{51}$$

$$\sum_{j=1}^{N-1} \Delta z_{j+1/2} \epsilon_{j+1/2} = \sum_{j=1}^{N} \Delta z_j \epsilon_j \tag{52}$$

Such constraints are satisfied by making the following choice of discretizations

$$\mathrm{Sh}_{j+1/2} = \frac{\left(\delta_z \overline{u}\right)^{n+1/2}_{j+1/2}}{\Delta z_{j+1/2}} \left(K_{j+1/2} \frac{\left(\delta_z \overline{u}\right)^{n+1,\star}_{j+1/2}}{\Delta z_{j+1/2}} - (a_p w_p)_{j+1/2} \left(u^p_{j+1/2} - \overline{u}^{n+1,\star}_j\right) \right) \tag{53}$$

$$\mathcal{B}_{j+1/2} = -K^{\phi}_{j+1/2} \left(N^2\right)^{n+1,\star}_{j+1/2} + (a_p w_p)_{j+1/2} \left(b_{\mathrm{eos}}\left(\overline{\phi}^p_{j+1/2}\right) - b_{\mathrm{eos}}\left(\overline{\phi}^{n+1,\star}_j\right) \right) \tag{54}$$

$$\epsilon_j = \frac{\Delta z_{j+1/2} \epsilon_{j+1/2} + \Delta z_{j-1/2} \epsilon_{j-1/2}}{2 \Delta z_j} \tag{55}$$

further assuming that $\epsilon_{1/2} = \epsilon_{N+1/2} = 0$. Considering the discretizations Equations 53, 54, and 55, the total energy budget of the water column reads

$$\sum_{j=1}^{N}\Delta z_j\frac{\left(c_p\overline{\theta}-z\overline{b}+\overline{u}^2/2\right)_j^{n+1}-\left(c_p\overline{\theta}-z\overline{b}+\overline{u}^2/2\right)_j^{n}}{\Delta t}+\sum_{j=1}^{N-1}\Delta z_{j+1/2}\frac{k_{j+1/2}^{n+1}-k_{j+1/2}^{n}}{\Delta t}$$
$$=\overline{u}_{N+1/2}^{n+1/2}\frac{\tau_x}{\rho_0}+\left(c_p-\frac{\alpha g\Delta z_{N+1/2}}{2}\right)\overline{w'\theta'}_0-\frac{\beta g\Delta z_{N+1/2}}{2}\overline{w'S'}_0-\mathcal{G}_N+\mathcal{G}_1 \tag{56}$$

ensuring that total energy is conserved up to boundary forcings. We check in the following section that this budget is indeed recovered in our SCM code.

5. SCM Evaluation and Parameterization Impacts

In this section, we test on the two idealized cases the sensitivity of the scheme to the formulation of TKE transport, energetic consistency, boundary conditions, mass-flux transport of horizontal momentum, and small plume area assumption. We also quantify energy biases of inconsistent formulations, including double-counting errors due to inconsistent boundary conditions. The constants c_m, c_ϵ, c_k used in the ED terms are the same as the constants used in the TKE equation of the LES model. We performed a preliminary calibration of the parameters using a MCMC Bayesian estimation algorithm (close to Souza et al., 2020) conditioned on our LES data. The Maximum A Posteriori estimate, similar to optimal parameters that could be obtained from an optimization algorithm, is $C_{\text{ent}} = 0.94, C_{\text{det}} = 1.4, a = 0.51, b = 0.85, b' = 0.98, C_u = 0.16, a_p^0 = 0.22, \delta_0 = 1.68, w_p^0 = -7.3 \times 10^{-8}$ ms^{-1}. A more detailed tuning and uncertainty quantification of the parameters, using statistical method (e.g., Couvreux et al., 2021; Dunbar et al., 2021; Souza et al., 2020) is left for future studies. Sensitivity to time step and number of vertical levels is presented in Appendix E.

5.1. Impact of the Energetic Consistency and Comparison to EVD

In Part I, we exposed that energy biases could arise from two sources: either from inconsistent TKE equation in which MF related sources of energy were missing, or from boundary conditions inconsistent with the ED + MF decomposition, leading to spurious energy fluxes at the surface. To quantify these biases, four different configurations of EDMF against LES data are tested, and we also compare to the Enhanced Vertical Diffusion (EVD) scheme for reference. The different configurations are detailed below.

EDMF-Energy: this is the default configuration. It consists of the previously detailed EDMF scheme in which the TKE equation consistently includes the contribution of MF terms to energy transfers as detailed in Equation 4. Moreover, simple consistent boundary conditions, leading to a zero MF temperature flux, are chosen (see Part I for details)

$$\begin{cases}\theta_p|_0=\overline{\theta}|_0\\ -K_\phi\partial_z\overline{\theta}|_0=\overline{w'\theta'}|_0\end{cases} \tag{57}$$

EDMF-TKE-inconsistent: In this configuration we use the following TKE equation instead of Equation 4,

$$\partial_t k+\partial_z\left(-K_k\partial_z k\right)=-K_\phi\partial_z\overline{b}+K_u\left(\partial_z\overline{\boldsymbol{u}}_h\right)^2-\overline{\epsilon} \tag{58}$$

This setup would result from a coupling between ED and MF, treated as if they were independent schemes. It is not energetically consistent, since the contributions of MF to the buoyancy and shear production of TKE are missing (Part I). Boundary conditions are the same as for EDMF-Energy.

EDMF-boundary-inconsistent: this configuration uses the consistent TKE Equation 4, along with the type of boundary conditions used for example in Pergaud et al. (2009), adapted from Soares et al. (2004),

$$\begin{cases}\theta_p|_0=\overline{\theta}|_0+\beta_{\text{P09}}\dfrac{\overline{w'\theta'}|_0}{\sqrt{k|_0}}\\ -K_\phi\partial_z\overline{\theta}|_0=\overline{w'\theta'}|_0\end{cases} \tag{59}$$

where $\beta_{\text{P09}} = 0.3$ is a numerical constant. These boundary conditions are not consistent with the physical flux imposed in Equation 39 when $w_p|_0$ is not zero, and are equivalent to prescribing the unphysical heat flux

$$T_{E_{i+p}}|_0 = c_p\overline{w'\theta'}|_0 + c_p\overline{w'\theta'}|_0\frac{a_p|_0 w_p|_0\beta_{\text{P09}}}{\sqrt{k|_0}} \tag{60}$$

where the second term of the r.h.s. is a spurious source of energy. This bias is due to an inconsistent partitioning of the physical boundary flux $c_p\overline{w'\theta'}|_0$ into ED and MF fluxes.

The objective of using this configuration is not to show whether Pergaud et al. (2009) parameterization is inconsistent or not. It is to point out that such type of boundary conditions, used at $z = 0$, can lead to inconsistent energetics. Finally, imposing $w_p|_0 = 0$ to fix this inconsistency is not satisfactory, since it leads to a mathematically inconsistent boundary condition (see Section 2.4.2 of Perrot et al., 2025).

EDMF-boundary-consistent: this configuration uses the consistent TKE Equation 4. We use boundary conditions where the bias in EDMF-boundary-inconsistent is corrected via a modification of the ED flux to avoid double-counting of energy at the boundary:

$$\begin{cases} \theta_p|_0 = \overline{\theta}|_0 + \beta_{\text{P09}}\dfrac{\overline{w'\theta'}|_0}{\sqrt{k|_0}} \\ -K_b|_0\partial_z\overline{\theta}|_0 = \overline{w'\theta'}|_0 - a_p|_0 w_p|_0\left(\theta_p|_0 - \overline{\theta}|_0\right) = \left(1 - \beta_{\text{P09}}\dfrac{a_p|_0 w_p|_0}{\sqrt{k|_0}}\right)\overline{w'\theta'}|_0 \end{cases} \tag{61}$$

TKE + EVD: This last configuration is the standard "TKE and Enhanced Vertical Diffusivity (EVD)" scheme used routinely in the Nucleus for European Modeling of the Ocean (NEMO, Madec et al., 2019). It relies on an ED-only closure based on the prognostic TKE Equation 58. Moreover, at depths where $N^2 < 0$, the eddy-diffusivity coefficient is enhanced to the arbitrary value $K_\phi = 10\ \text{m}^2\text{s}^{-1}$. The eddy-viscosities $K_u = K_k$ are unaffected, and still computed via the prognostic TKE equation (see Appendix A).

5.1.1. Instantaneous Turbulent Profiles

The comparison of the five aforementioned configurations are plotted for the cases FC500 and W005_C500 on Figures 6 and 7.

TKE + EVD exhibits a noticeable different surface temperature compared to all the other EDMF schemes. The cooling flux imposed at the surface leads to a destabilization of the surface temperature profile and an activation of EVD. The high value of eddy-diffusivity imposes a too high mixing of surface temperature, responsible for the bias. For EDMF models the ED flux dominates near the surface (dashed-dotted lines on panels 6(b) and 7(d)). However, this ED flux is computed via a TKE scheme, leading to much smaller eddy-diffusivity values than EVD, and consequently more negative gradients of temperature at the surface. These strongly unstable profiles at the surface appear more realistic when compared to LES.

TKE + EVD necessarily produces unstable (near-neutral) temperature profiles (Figures 6a and 7a) collocated at depth where the temperature flux is positive, since by design TKE + EVD can only allow down-gradient fluxes. As a contrary, LES profiles exhibit stable profiles of temperature from $z/h \simeq -0.4$ towards the base of the mixed layer, a robust feature of convective boundary layers (Zhou et al., 2018). Moreover, TKE + EVD fails to reproduce accurately the vertical entrainment zone at the base of the mixed layer (e.g., Garcia & Mellado, 2014), in which penetrative convection, caused by plumes overshooting their neutral level, generates negative temperature flux and sharpens the temperature gradients. The lack of penetrative convection is known to reduce the deepening rate (e.g., chap. 6, Garratt, 1994), and results in a $\sim$20% underestimation of the MLD by TKE + EVD compared to LES. The underestimation of vertical entrainment fluxes (and hence penetrative convection) in ED-only models is sometimes mistakenly attributed to the absence of non-gradient or counter-gradient terms (e.g., Giordani et al., 2020). However, in the vertical entrainment zone where penetrative convection occurs, negative temperature fluxes align with positive temperature gradients, which can indeed be accurately represented by eddy-diffusivity models if specific formulations for the entrainment zone are applied (e.g., Bretherton &

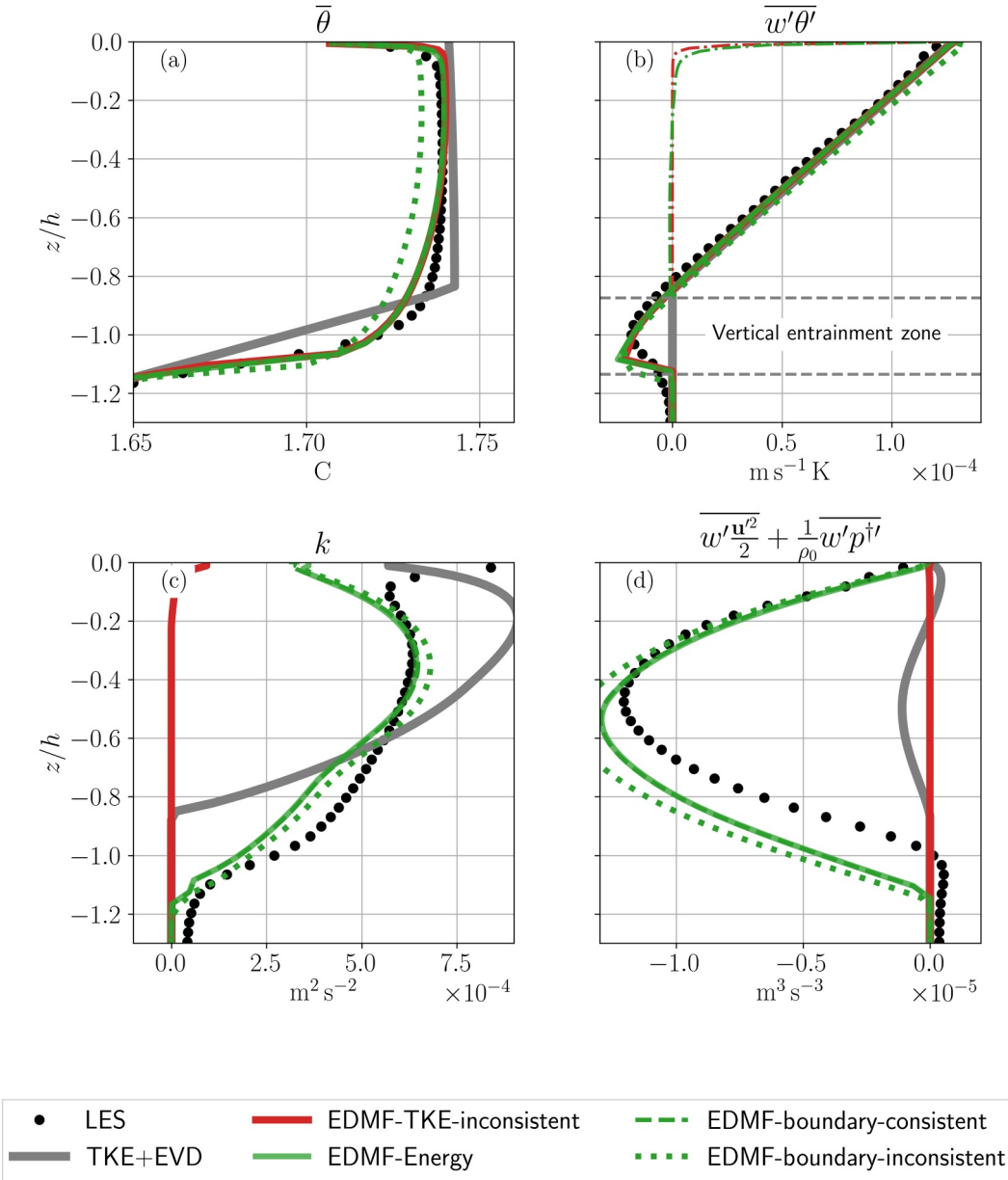

Figure 6. Mean and turbulent profiles for the case FC500 case after 72h of simulation: (a) temperature, (b) temperature flux, (c) turbulent kinetic energy (TKE), (d) TKE flux. Large Eddy Simulations data (black dots), TKE + EVD scheme (gray line), EDMF-TKE-inconsistent (red line), EDMF-Energy (green line), EDMF-boundary-consistent (green dashed) and EDMF-boundary-inconsistent (green dotted) are represented, along with the ED contribution to the temperature fluxes (panel b) for EDMF-TKE-inconsistent (dashed-dotted red) and EDMF-Energy (dash-dotted green). In all panels, the plain green and dashed green lines are overlapping.

Park, 2009). Conversely, both EDMF-TKE-inconsistent and EDMF-Energy models perform similarly in capturing temperature profiles and fluxes. The absence of a noticeable effect of the TKE energetic consistency on these profiles is a consequence of the small value of the eddy-diffusivity fluxes (dashed-dotted thin lines) in the mixed layer. Associated eddy-diffusivity reaches at most 0.1 $\mathrm{m^2\ s^{-1}}$. Solutions computed using EDMF-Energy and EDMF-boundary-consistent coincide, whereas EDMF-boundary-inconsistent exhibits a cool bias of $\simeq 0.01°\,C$ on temperature profiles (Figures 6a and 7a) due to the spurious flux imposed at the surface. Since buoyancy in the mixed layer scales with $N^2 h$ (Garratt, 1994) this bias is expected to increase with the MLD.

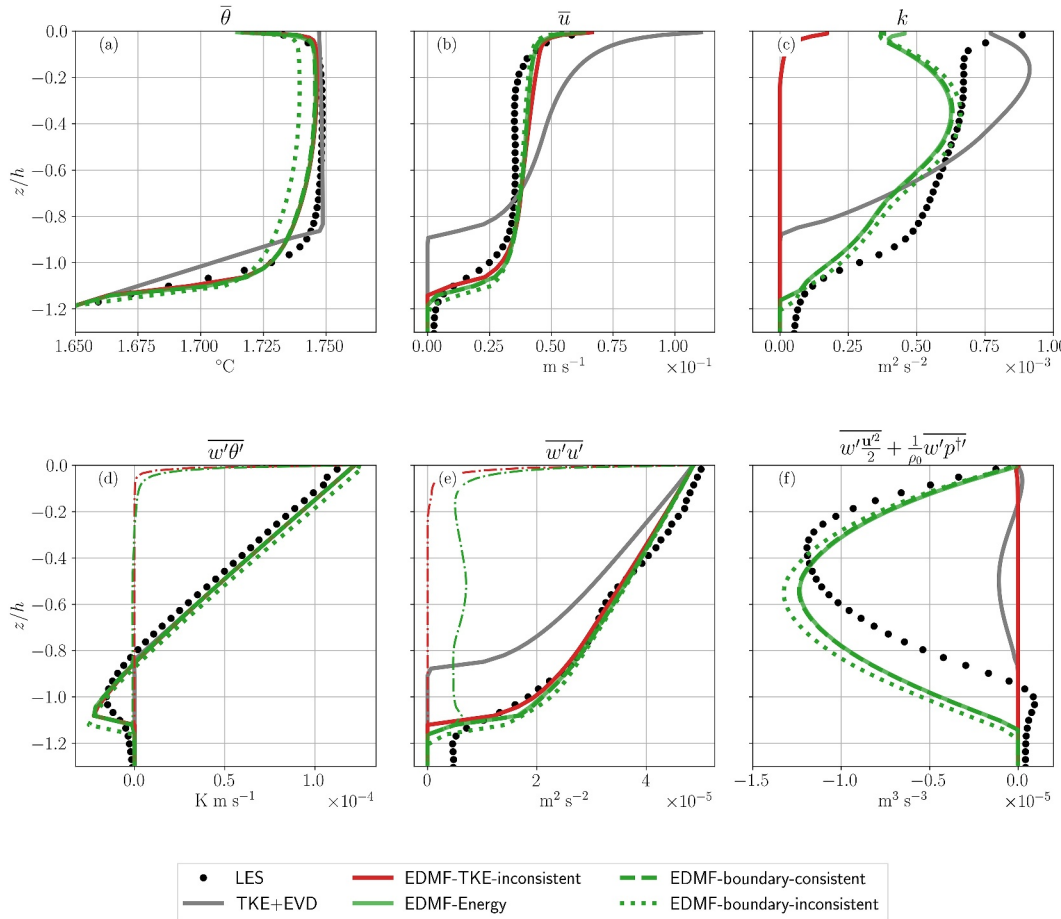

Figure 7. Same as Figure 6 for the case W005_C500 except for Panel (b): mean zonal velocity, and Panel (e): zonal velocity flux (plain lines represent the full Eddy-Diffusivity Mass Flux flux, and dashed-dotted lines the ED contribution to this flux). In all panels, the plain green and dashed green lines are overlapping.

When considering the TKE profile (Figures 6c and 7c), TKE + EVD captures the correct order of magnitude compared to LES. However, its vertical distribution is not deep enough. EDMF-TKE-inconsistent fails to reproduce TKE due to energetic inconsistency. Indeed, looking at temperature and velocity fluxes (Figures 6b and 7d,e) allows to infer that the losses of resolved energy due to buoyancy and shear are dominated by the MF contributions. However, such contributions are not included as sources of TKE for the EDMF-TKE-inconsistent scheme, leading to the very low levels of TKE observed in the simulation. The three models including a consistent TKE equation (EDMF-Energy, EDMF-boundary-consistent, EDMF-boundary-inconsistent) can reproduce accurate profiles of TKE. The main discrepancies between these configurations and LES arise close to the surface and at the base of the mixed layer, and could be due to TKE boundary condition modeling.

Regarding the vertical transport of TKE (Figures 6d and 7f), EDMF-TKE-inconsistent is not able to reproduce the LES profile. TKE + EVD displays the correct shape, however, the magnitude is approximately 10 times less than the reference profile. EDMF-Energy, EDMF-boundary-consistent and EDMF-boundary-inconsistent are able to reproduce the profile, with a shift downwards of a few percent of the MLD h.

5.1.2. Vertically Integrated Energy Budgets

In Figure 8, we show the vertically integrated energy budget of the SCM for the case W005_C500 (FC500 is similar), namely the quantity

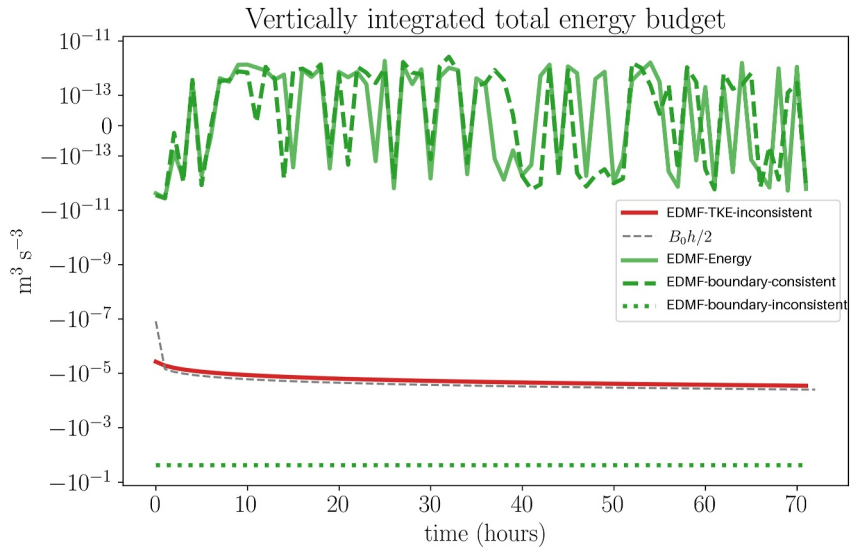

Figure 8. Time series of the vertically integrated energy budget (62) for the case W005_C500 (see text for details).

$$\int_{-H}^{0} \partial_t (E_k + k + E_{i+p})\, \mathrm{d}z + [T_{E_k} + T_k + T_{E_{i+p}}]_{z=-H}^{z=0} \tag{62}$$

where the different energy reservoirs and fluxes are introduced in Equations 4–6, and the boundary operator is defined as $[X]_{z=-H}^{z=0} = X(z=0) - X(z=-H)$. As expected, EDMF-Energy conserves energy up to round-off errors ($\pm 10^{-12}$ m^3 s^{-3}) whereas EDMF-TKE-inconsistent exhibits an energy loss of about 10^{-5} m^3 s^{-3} corresponding to

$$\int_{-H}^{0} \left(-a_p w_p \left(b_p - \overline{b}\right) + a_p w_p \left(\boldsymbol{u}_{h,p} - \overline{\boldsymbol{u}}_h\right) \cdot \partial_z \overline{\boldsymbol{u}}_h\right) \mathrm{d}z \tag{63}$$

which scales with $B_0 h/2$ in this buoyancy-dominated convection experiment. EDMF-boundary-inconsistent exhibits an important bias of 10^{-1}m^3 s^{-3} due to a spurious internal energy flux at the boundary (see Equation 60 and Section 4.5 of Perrot et al. (2025)). As expected, the modification of the boundary condition in EDMF-boundary-consistent allows to recover an energy-conserving scheme.

5.2. Impact of TKE Transport

In Figure 9, we compare the new TKE transport parameterization introduced in Section 2 to the closures proposed by Witek et al. (2011) and by Han and Bretherton (2019):

$$\overline{w' \frac{\boldsymbol{u}' \cdot \boldsymbol{u}'}{2}} = \underbrace{-K_k \partial_z k}_{\text{ED}} + \underbrace{\overbrace{a_p w_p (k_p - k)}^{\text{Han \& Bretherton 2019}} + \overbrace{\frac{1}{2} a_p w_p^3}^{\text{Witek et al. 2011}} + \frac{a_p w_p}{2} \|\boldsymbol{u}_{h,p} - \overline{\boldsymbol{u}}_h\|^2}_{\text{new EDMF}} \tag{64}$$

Moreover, we use a different plume TKE equation than the one used in Han and Bretherton (2019),

$$a_p w_p \partial_z k_p = \underbrace{\overbrace{E(k - k_p)}^{\text{Han \& Bretherton 2019}} + E\left(\frac{1}{2}\|\boldsymbol{u}_p - \overline{\boldsymbol{u}}\|^2\right) - a_p \epsilon_p}_{\text{new EDMF}} \tag{65}$$

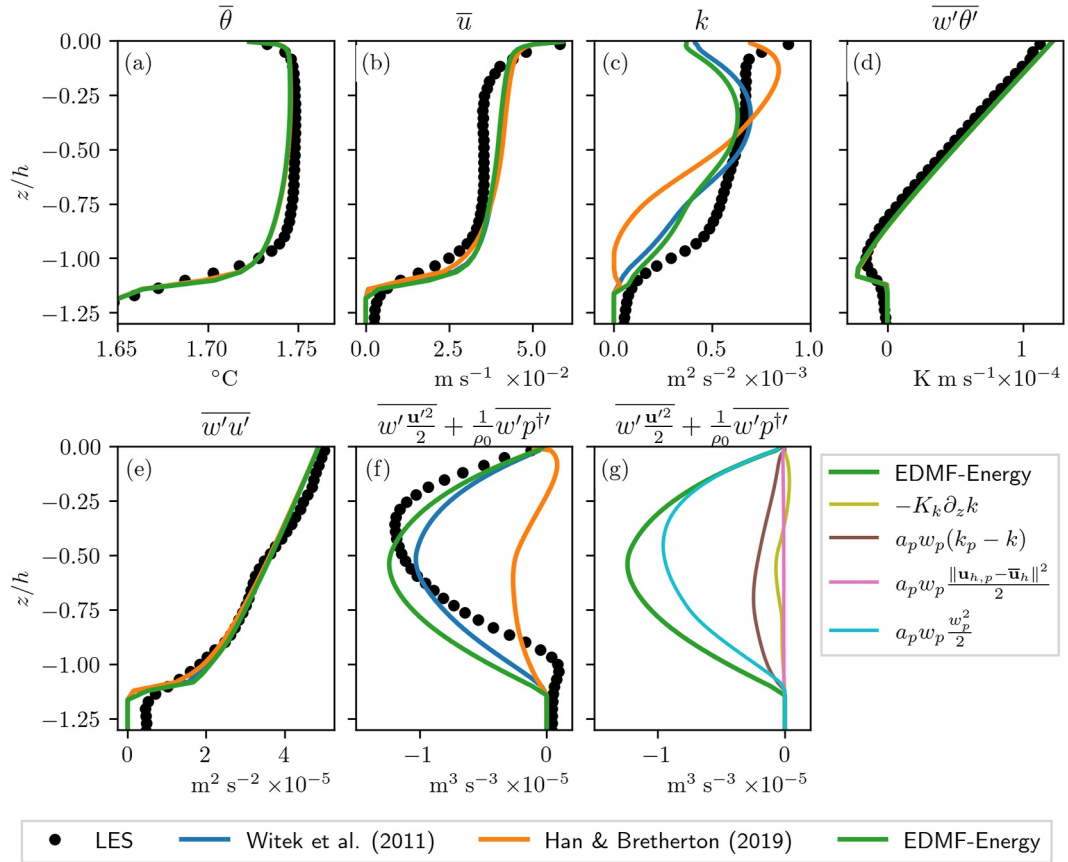

Figure 9. Instantaneous turbulent moments for the case the W005_C500 after 72h of simulation: (a) temperature, (b) zonal velocity, (c) turbulent kinetic energy (TKE), (d) temperature flux, (e) zonal velocity flux, (f) TKE flux. Large Eddy Simulations data (black dots) is represented, as well as three energetically consistent Eddy-Diffusivity Mass Flux scheme differing only by their parameterization of TKE transport: Witek et al. (2011) (blue line), Han and Bretherton (2019) (orange line) and the new formulation (green line). On panel (g), the TKE flux of the configuration EDMF-Energy is decomposed based on the contribution of the parameterization exposed in Equation 64. On panel (a), blue, green and orange lines are overlapping. On panels (b), (d) and (e), the blue and green lines are overlapping.

The choice of TKE transport seems to have a negligible impact on temperature, temperature fluxes, velocity and momentum fluxes. When looking at TKE fluxes (Figure 9f), all parameterizations reproduce the bell-shape but exhibit a consistent shift downwards of approximately 0.1 h. Concerning the minimum of the TKE flux (Figure 9f), Han and Bretherton (2019) parameterization exhibits a bias of 80% compared to LES. In contrast, Witek et al. (2011) underestimate (in absolute value) the minimum of about 10%. In Figure 9g, we show the different terms of TKE flux (64) for EDMF-Energy. 90% of the flux is explained by $1/2 a_p w_p^3$, about 10% by $a_p w_p(k_p - k)$. The remaining terms are small, which could be expected since W005_C500 is in a convection-dominated regime.

Transport of TKE has a direct effect on the profile of TKE (Figure 9c). The surface production of TKE appears to be insufficiently redistributed for Han and Bretherton (2019) schemes, resulting in insufficient levels of TKE within the lower half of the mixed layer. The more realistic TKE transports of Witek et al. (2011) and of the new scheme lead to a better distribution of the TKE inside the mixed layer. The surface TKE bias, may be related to boundary condition choices that should be further investigated. Our implementation of Han and Bretherton (2019) reproduces well the shape of TKE plotted in Figure 4 of their paper; but their implementation exhibits a clear lack of production of TKE contrary to the results we show in Figure 9. This could suggest missing TKE production terms in their implementation.

We show in Figure 10 different plume variables conditionally sampled from LES (see Section 3.3 for details). They are compared with plume variables computed from different EDMF configurations. We advocate that this comparison can be used for qualitative understanding rather than quantitative evaluation of the schemes, since

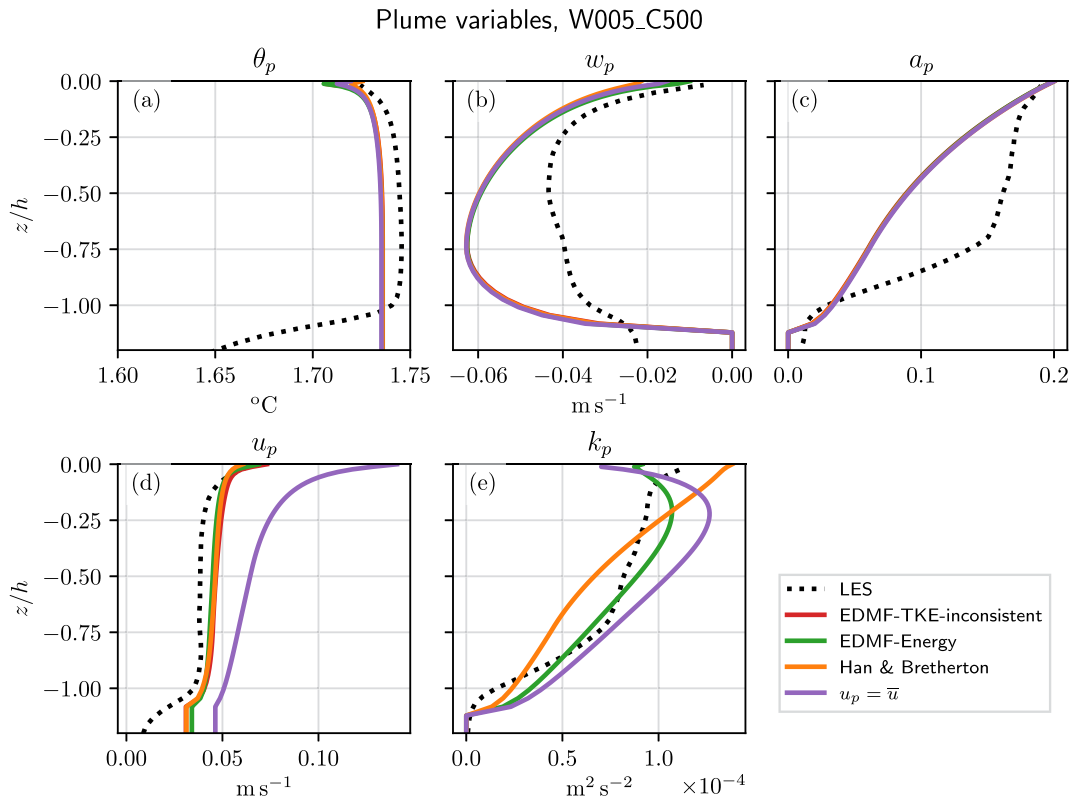

Figure 10. Vertical profiles of plume variables after 72 hr of simulation for the case W005_C500, computed from different configurations: EDMF-TKE-inconsistent (red), EDMF-Energy (green), EDMF-Energy with Han and Bretherton (2019) parameterization of Turbulent Kinetic Energy transport (orange), EDMF-Energy with no MF momentum flux, that is $u_p = \overline{u}$ (purple). The black dotted line represents plumes identified in Large Eddy Simulations, using the conditional averaging presented in Section 3.3.

SCM plume profiles are sensitive to the model's free parameters, and LES plume profiles are sensitive to the conditional sampling parameters. All the SCM models produce similar plume temperature, vertical velocity, and fractional area. Compared to EDMF-Energy, the EDMF model imposing $u_p = \overline{u}$ (described in next section) exhibits higher plume TKE levels (panel 10-(e)) due to the vanishing term $E|u_p - \overline{u}|^2$ in the k_p budget (65) (since $w_p < 0$, this term is a net sink of k_p for increasing z). Han and Bretherton (2019) did not include dissipation in their model, leading to even higher levels of k_p.

5.3. Impact of Horizontal Momentum Transport

In Figure 11, we examine the impact of the mass-flux on horizontal momentum transport by comparing a simulation in which $\overline{w'\boldsymbol{u}_h'}^{\mathrm{MF}} = 0$ or equivalently $\boldsymbol{u}_{h,p} = \overline{\boldsymbol{u}}_h$ (a choice made in several studies, e.g. Cohen et al., 2020; Giordani et al., 2020; Tan et al., 2018) to a simulation where the horizontal velocity plume model $\boldsymbol{u}_{h,p}$ is explicitly parameterized according to Table 1, and leads to $\overline{w'\boldsymbol{u}_h'}^{\mathrm{MF}} \neq 0$.

The main effect of MF on horizontal velocities is to increase the momentum flux, which in turn produces more mixing of the zonal velocity compared to the velocities computed with ED-only momentum flux. According to the reference LES the well-mixed profile of $\overline{u}$, resulting from non-zero MF momentum flux, is more realistic.

Momentum transport does not seem to have an important impact on TKE in this case. This can be explained by the fact that W005_C500 depicts a convection-dominated regime; thus TKE is mainly produced by buoyancy, and the flux of TKE is dominated by the w_p^3 term.

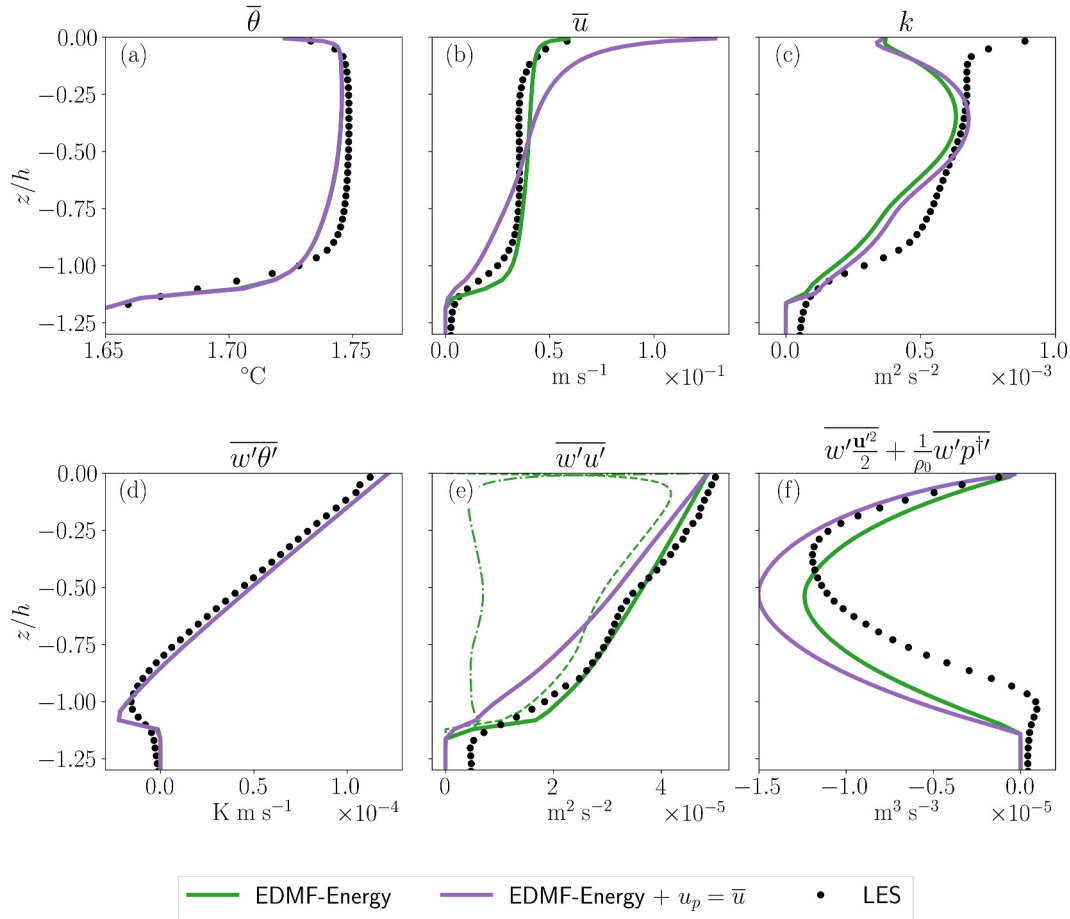

Figure 11. Mean and turbulent profiles for the W005_C500 case after 72h of simulation: (a) temperature, (b) zonal velocity, (c) turbulent kinetic energy (TKE), (d) temperature flux, (e) velocity flux, (f) TKE flux. In green: EDMF-Energy configuration. In purple: EDMF-Energy where we imposed $\boldsymbol{u}_{h,p} = \overline{\boldsymbol{u}}_h$, leading a zero MF contribution to momentum transport $\left(\overline{w'\boldsymbol{u}'_h}^{\mathrm{MF}} = 0\right)$. Zonal velocity flux (panel e) has been divided into ED (green dash-dotted) and MF (green dashed) contributions for the EDMF-Energy parameterization. On panels (a) and (d), the green and purple lines are overlapping.

When $u_p = \overline{u}$, turbulent transport of TKE (panel 11-(f)) is negatively increased because k_p is increased (see Figure 10). Indeed, in such case the energy loss due to $E\left(\|\boldsymbol{u}_{h,p} - \overline{\boldsymbol{u}}_h\|^2/2\right)$ vanishes, in the k_p budget (65), leading to higher values of k_p.

5.4. Impact of Small Area Assumption

In Section 3.3, analysis of LES revealed that the assumption $a_p \ll 1$ was not fully satisfied. This small-area assumption can be relaxed with no additional complexity if the subplume fluxes $\overline{w'_p\phi'_p}$ $(\phi = \theta, S, u, v)$ are still neglected (Tan et al., 2018). A summary of the EDMF-Energy parameterization in such a regime is presented in Table 1. On Figure 12 we compare instantaneous profiles from EDMF-Energy to EDMF-Energy where a_p is not assumed small.

Relaxing the small area assumption mainly affects the minimum of the TKE transport (Figure 12-f), reducing by 10% which roughly corresponds to the rescaling coefficient $\sigma = 1/(1 - a_p)$. As a consequence TKE is less redistributed on the vertical, leading to slightly higher TKE close to the surface and reduced TKE in the interior. Other mean fields and fluxes do not seem affected. However, the influence of the small plume area would be more clearly seen in the gray zone of convection, that is when the horizontal size of convective structures approach the horizontal size of the LES domain (Honnert, 2022). For 3D implementations of the parameterization at resolution lying within the gray zone, the dependency of parameters to resolution should be assessed.

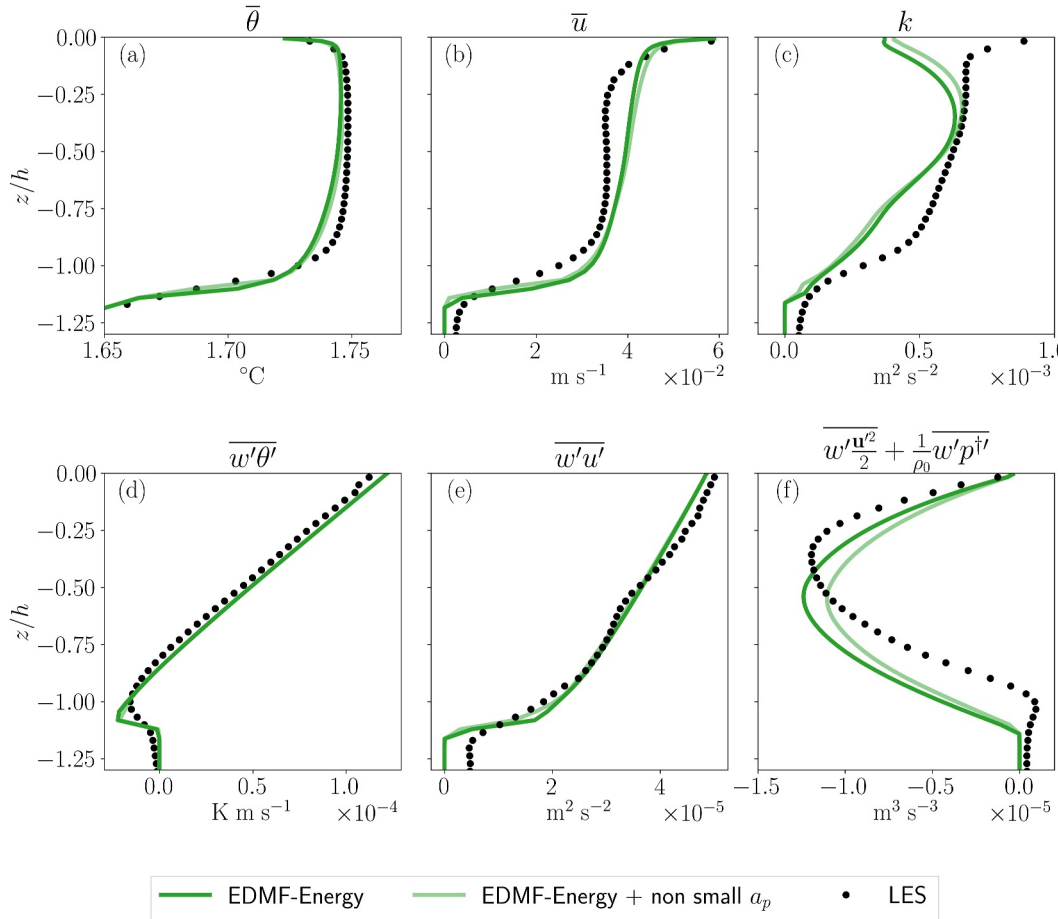

Figure 12. Mean and turbulent profiles for the W005_C500 case after 72h of simulation: (a) temperature, (b) zonal velocity, (c) turbulent kinetic energy (TKE), (d) temperature flux, (e) zonal velocity flux, (f) TKE flux. Solid green line: EDMF-Energy (with small area assumption). Light green line: EDMF-Energy where a_p is not assumed small.

5.5. Realistic Case: Hymex/ASICS-MED Campaign

We now move to more realistic situations corresponding to a sequence of strong convective events which were documented in the Northwestern Mediterranean during the winter 2013 of the HyMeX/ASICS-MED experiment at the LION buoy. These events correspond to localized oceanic deep convection (Marshall & Schott, 1999) for which the water column is typically mixed over thousands meters, sometime down to the seafloor. These winter events are common in the Mediterranean Sea as well as in the Labrador and Greenland Seas, and are of great importance for deep water formation and their overall influence on basin scale dynamics. The ASICS-MED experiment was also used in Giordani et al. (2020), and we use a similar setup here (similar vertical grid, similar initial conditions, similar corrected surface fluxes from Caniaux et al. (2017)). We also use the same reference observational data, which advantageously combine LION mooring data and measurements originating from an array of gliders, Argo floats and CTD casts deployed around the mooring during ASICS-MED survey. The numerical experiments are performed with a SCM similar to Equation 1 but including additional Coriolis and solar penetration (using a standard Jerlov law) terms, and we use a nonlinear equation of state. We also include penalization terms in the SCM to enforce $w_p = 0$ at the ocean floor to account for the effect of the bottom (which is at a depth of 2400 m at the LION buoy). Thanks to the penalization term a no-slip boundary condition is imposed at the bottom and a no-gradient condition is imposed for tracers. The vertical grid resolution ranges from 1 m near the surface to 150 m near the bottom located at $z = -2400$ m. Parameters of the TKE scheme are set to the standard values used in NEMO (Nucleus for European Modeling of the Ocean, Madec et al., 2019), $\boldsymbol{c} = (c_m, c_\epsilon, c_k) = \left(0.1, \frac{\sqrt{2}}{2}, 0.1\right)$.

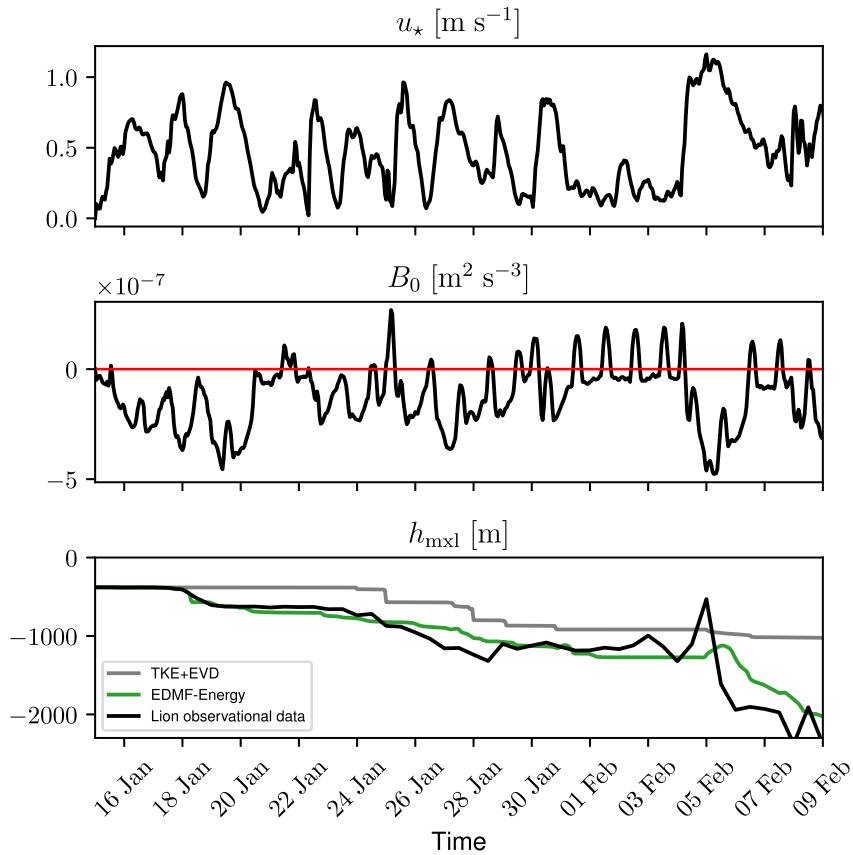

Figure 13. Time series of the friction velocity $u_\star$ (m s^{-1}, top panel) and surface buoyancy flux B_0 (m^2 s^{-3}, middle panel) computed from atmospheric forcings. Time series of mixed layer depth h_{mxl} (m, bottom panel) obtained from observations around the LION buoy (black line) and from single-column numerical experiments using TKE + EVD (solid gray line) and EDMF-Energy (solid green line).

A series of 25-day numerical simulations were carried out starting from 15 January 2013. The surface boundary conditions are shown in Figure 13. In particular, very strong cooling events occurred during the period of interest. Two simulations were made systematically with an eddy-diffusivity term activated. A first simulation was done with Enhanced Vertical Diffusion (referred to as TKE + EVD) which is the standard practice for climate simulations using NEMO, a second one using a mass flux scheme on tracers, horizontal momentum, and with the additional terms for energetic consistency in the TKE equation (referred to as EDMF-Energy). To get a more concrete idea of the improvements brought about by the mass flux scheme over the usual practice for NEMO applications (TKE + EVD), we show in Figure 13 (bottom panel) the temporal evolution of the MLD h_{mxl} computed from observational data and single-column numerical simulations. h_{mxl} is defined as the depth where the following criterion is met

$$\int_{h_{\mathrm{mxl}}}^{z_{\mathrm{ref}}} \partial_z \theta \, dz = \delta\theta \tag{66}$$

with $z_{\mathrm{ref}} = -300\,\mathrm{m}$ and $\delta\theta = 0.05\,\mathrm{K}$. This choice of reference level is consistent with the one used in Houpert et al. (2016) also with LION observational data. Moreover, the mixed layer depths obtained by applying (66) on the data (see black curve in Figure 13) are directly comparable with the ones shown in Waldman et al. (2017) (see their Figure 4). Panel (c) in Figure 13 illustrates the fact that the MLD is significantly better represented by the EDMF-Energy scheme than by the TKE + EVD approach. Moreover, a direct comparison with temperature (resp. salinity) from observational data is shown in Figure 14 (resp. Figure 15) over the period from January 15 to 9 February 2013. In particular, several phases can be identified during the experiment (e.g., Coppola et al., 2017; Waldman et al., 2017): (a) in the period January 15 to 25, 2013, winter convection starts to deepen the mixed layer

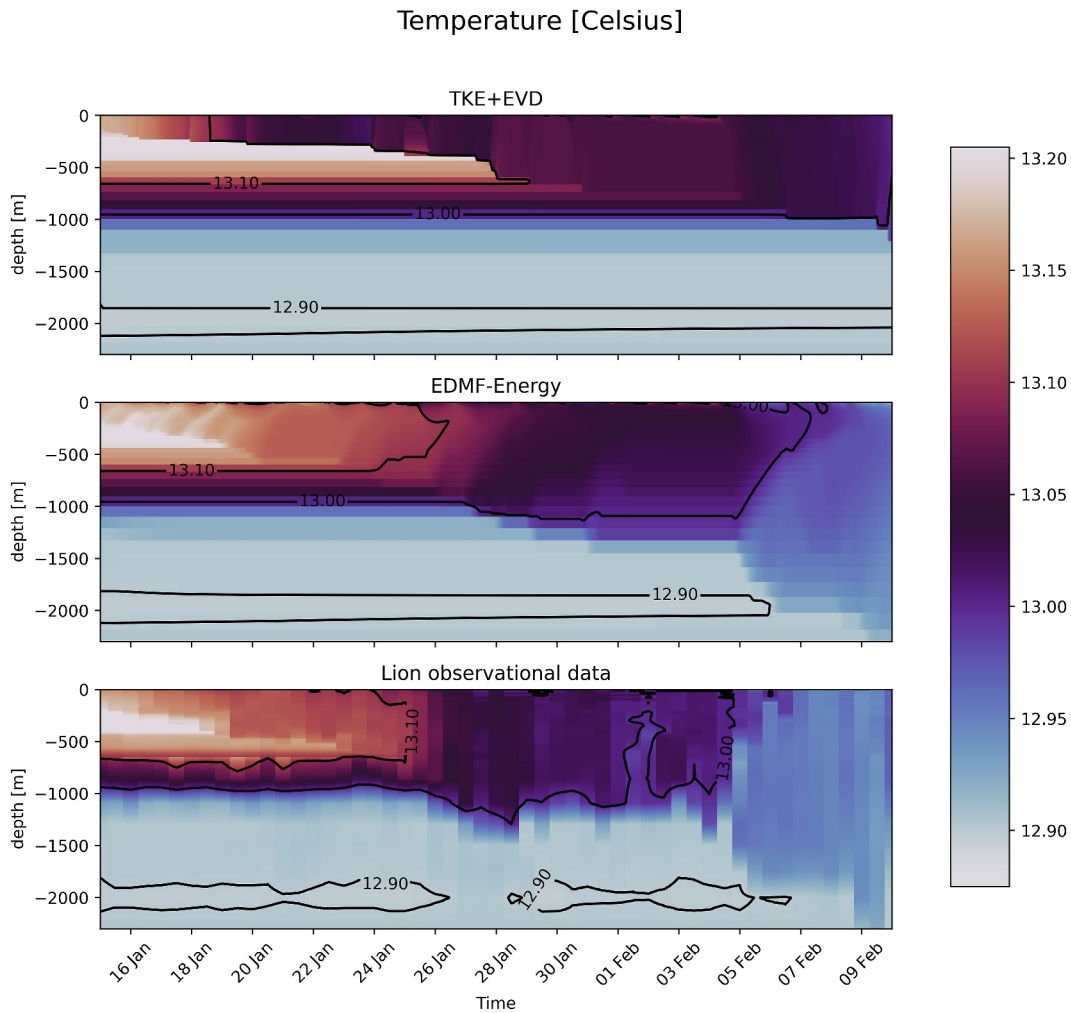

Figure 14. Potential temperature (°C) time series as a function of depth for single-column numerical experiments using an eddy-diffusivity closure with enhanced vertical diffusion (TKE + EVD, top panel) or using an energetically consistent Eddy-Diffusivity Mass Flux (EDMF-Energy, middle panel) and for observational data (bottom panel).

down to around −800 m to the point of eroding the Levantine intermediate waters (Estournel et al., 2016) (b) in the period January 26 to 29, 2013, the mixed layer keeps thickening to the depth of the western Mediterranean deep water (≈ −1250 m) (c) in the period February 4 to 9, 2013, a new intense convective event associated with a strong Mistral wind event contributes to deepen the mixed layer down to the bottom (reached on February 9). This is followed by a restratification phase involving horizontal processes that cannot be represented in our SCM formalism which explains why we do not analyze solutions beyond February 9. Similarly, the delay between observations and EDMF-Energy regarding the restratification peak visible on February 5 could be due to horizontal advection caused by the intense wind forcing.

In general, as illustrated by the temperature profiles in Figure 14 and the temporal evolution of the MLD in Figure 13, the EDMF-Energy simulation correctly represents these three phases, notably with a very pronounced erosion of the intermediate Levantine waters on 25 January 2013, and a destratification of the entire water column on 9 February 2013. This good agreement with observational data is also noticeable when looking at salinity (Figure 15). Conversely, in the TKE + EVD simulations, the timescales for the erosion of stratification are significantly slower than in the observations.

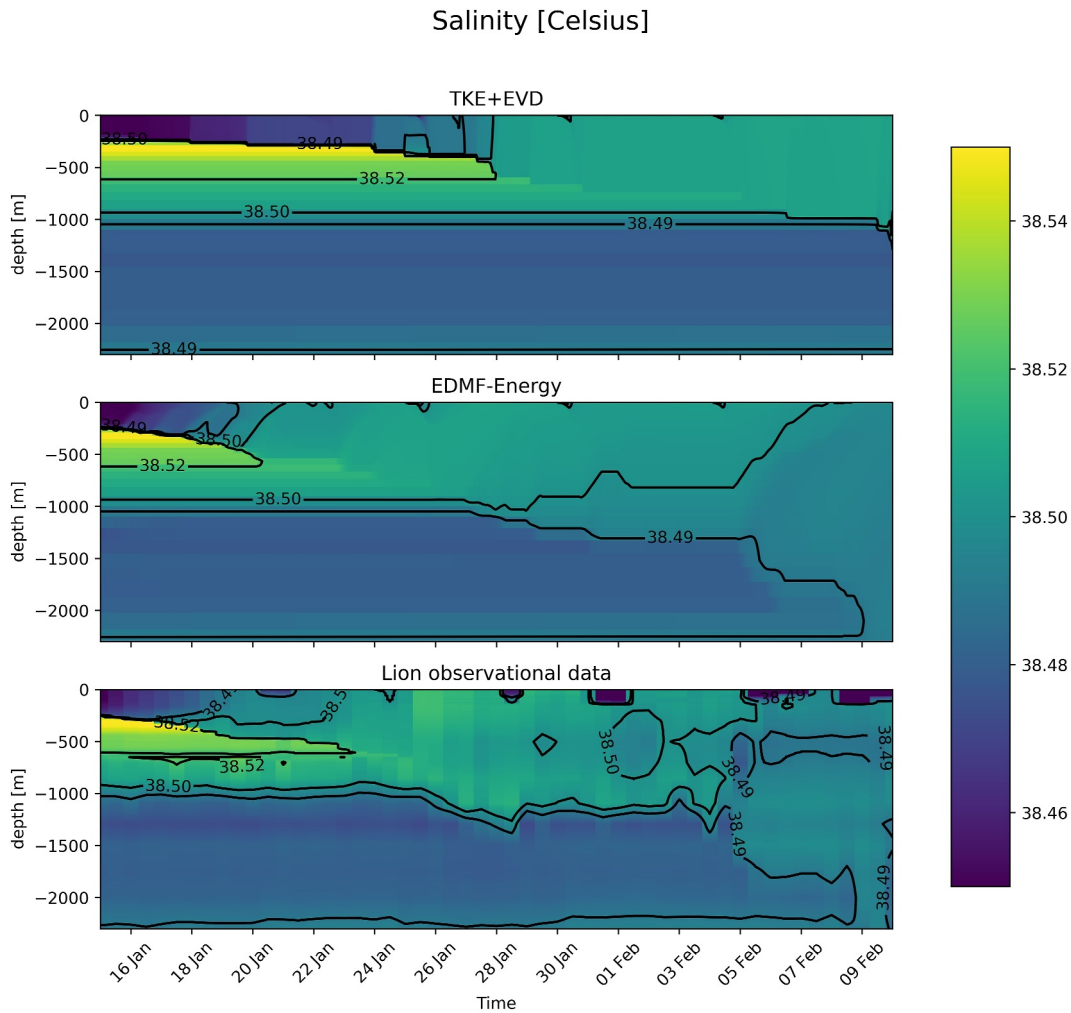

Figure 15. Same as Figure 14 but for salinity (psu).

6. Discussion and Conclusion

In this work, we used idealized LES of oceanic convection to analyze hypotheses and outputs of a novel Eddy-Diffusivity Mass-Flux parameterization in a Single-Column Model configuration, derived in Part I (Perrot et al., 2025). This energetically consistent parameterization is rather simple to implement, whether in a code with an existing "non-energetically consistent" EDMF scheme or, more generally, in any code relying on a prognostic TKE equation. The MF terms are obtained by solving a straightforward system of ODEs and take the form of vertical advection terms in the mean equations (see Appendix D for practical details). The proposed approach can also be applied in the case where the ED closure does not use TKE. In this case, it would require to add a prognostic or diagnostic TKE equation (even if it does not interact with the ED term) to enforce energetic consistency.

Using vertical-velocity based conditional sampling of LES, we found that stationarity of the mean convective plume is well satisfied. However, even if plume typical radius is small compared to the size of the horizontal domain, plumes typically cover 15% to 20% of the horizontal domain. Consequently, the assumption of small plume area can be criticized, and we provided and implemented a set of equations without such an assumption. This new set of equations do not exhibit additional computational complexity compared to the standard approaches. Thus we recommend its usage since it is valid whenever plume fraction is or is not small. Based on LES we also proposed a new EDMF closure for the turbulent transport of TKE which generalizes two existing approaches. We expose the subtleties of numerical implementation of the SCM, including fully consistent discrete energy budgets based on their continuous counterparts. This study highlights how energy considerations can unambiguously guide discretizations. Finally, we performed a series of sensitivity experiment to different modeling aspects regarding

energetic consistency, boundary conditions, transport of TKE, transport of horizontal momentum by MF and small plume area assumption. Temperature and flux of temperature profiles do not appear to significantly be affected by such choices, and the SCM reproduces LES profiles compared to TKE + EVD. Applying the EDMF concept to momentum fluxes seems necessary to generate realistic mixing of horizontal velocities and properly represent their fluxes (Section 5.3). The usage of an energetically consistent TKE equation and along with the new formulation of TKE transport is key to obtaining realistic TKE and turbulent transport of TKE profiles. We also quantify the energy loss of inconsistent formulations, due to either inconsistent TKE equation or inconsistent boundary conditions. Surprisingly, removing the assumption of small plume area (without modifying plume closures) seems to only affect the transport of TKE in the test cases presented. All these findings are based on idealized cases, where in particular ED fluxes are small explaining the apparently small impact of energetic consistency and TKE on the solutions. Thus, a further assessment of global 3D simulations is a necessary next step to understand the implications of energetic consistency. To further illustrate that the EDMF concept is a credible alternative to the traditional approaches used in the oceanic context (using e.g. an enhanced vertical diffusion) the proposed scheme is validated in a single-column configuration against observational data of oceanic convection from the LION buoy.

To implement and then assess the impact of this energetically consistent parameterization on realistic 3D oceanic simulations a calibration of the remaining "free" parameters must be achieved (Couvreux et al., 2021; Hourdin et al., 2017). It should be performed on parameters whose universality can sometimes be statistically assessed (Souza et al., 2020), and should be mathematically and physically constrained as much as possible.

Appendix A: Mixing Length and Dissipation Computations

For the oceanic applications detailed in this article, we have chosen a formulation of eddy-diffusivity and viscosity close to that used in the NEMO ocean model (Madec et al., 2019). The eddy-viscosity and diffusivity are classically assumed to be related to TKE by

$$K_u = K_k = c_m l_m \sqrt{k} \tag{A1}$$

$$K_\phi = K_u (\mathrm{Pr}_t)^{-1} \tag{A2}$$

with l_m a mixing length scale, Pr_t the non-dimensional turbulent Prandtl number, and c_m a constant ($c_m = 0.1$ in NEMO). The mixing length l_m is calculated in two steps by considering separately the length scales l_{up} and l_{dwn} associated respectively to upward and downward movements: (a) l_{up} and l_{dwn} are initialized assuming $l_{\mathrm{up}} = l_{\mathrm{dwn}} = \sqrt{2k}\tau_{\mathrm{ed}}$ with τ_{ed} a characteristic time equal to $1/N^2 = \left(\partial_z \overline{b}\right)^{-1}$ (b) a physical limitation is used to ensure that l_{up} and l_{dwn} do not exceed the distance to the top and the bottom of the mixed layer, this limitation amounts to controlling the vertical gradients of l_{up} and l_{dwn} such that they are not larger than the variations of depth (e.g., Madec et al., 2019). Once l_{up} and l_{dwn} are computed the mixing length is taken as $l_m = \min(l_{\mathrm{up}}, l_{\mathrm{dwn}})$. The turbulent Prandtl number is modeled by $\mathrm{Pr}_t = \min\left(\mathrm{Pr}_t^{\max}, \max(\mathrm{Ri}/\mathrm{Ri}_c, 1)\right)$ with $\mathrm{Ri} = N^2/\|\partial_z \overline{\mathbf{u}}_h\|^2$, $\mathrm{Pr}_t^{\max} = 10$ and $\mathrm{Ri}_c = 0.2$.

The viscous dissipation is parameterized as $\overline{\epsilon} = \frac{c_\epsilon}{l_\epsilon} k^{3/2}$, where $c_\epsilon = \sqrt{2}/2$ is a numerical constant and the dissipation length is $l_\epsilon = \sqrt{l_{\mathrm{up}} l_{\mathrm{dwn}}}$ (e.g., Gaspar et al., 1990).

Appendix B: Third Order Moment Computations

By definition we have

$$k = \overbrace{\frac{1}{2} a_e \|\boldsymbol{u}_e - \overline{\boldsymbol{u}}\|^2 + a_e k_e}^{a_e k_e^t} + \overbrace{\frac{1}{2} a_p \|\boldsymbol{u}_p - \overline{\boldsymbol{u}}\|^2 + a_p k_p}^{a_p k_p^t} \tag{B1}$$

$$\Rightarrow k_p^t - k_e^t = \frac{1}{1 - a_p}\left(k_p^t - k\right) \tag{B2}$$

thus

$$\mathrm{III}_e + \mathrm{III}_p + \mathrm{IV}_e + \mathrm{IV}_p = a_p w_p \left(k_p + \frac{1}{2}\|\boldsymbol{u}_p - \overline{\boldsymbol{u}}\|^2 \right) + a_e w_e \left(k_e + \frac{1}{2}\|\boldsymbol{u}_e - \overline{\boldsymbol{u}}\|^2 \right) \tag{B3}$$

$$= a_p w_p \left(k_p + \frac{1}{2}\|\boldsymbol{u}_p - \overline{\boldsymbol{u}}\|^2 - k_e - \frac{1}{2}\|\boldsymbol{u}_e - \overline{\boldsymbol{u}}\|^2 \right) \tag{B4}$$

$$= a_p w_p \left(k_p^t - k_e^t \right) \tag{B5}$$

$$= \frac{a_p}{1 - a_p} w_p \left(k_p^t - k \right) \tag{B6}$$

$$= \frac{a_p}{1 - a_p} w_p \left(k_p + \frac{1}{2}\|\boldsymbol{u}_p - \overline{\boldsymbol{u}}\|^2 - k \right) \tag{B7}$$

Appendix C: Derivation of Plume TKE Equation 14

Applying the plume averaging to TKE, and assuming entrainment/detrainment closure for horizontal advection terms, k_p budget can be derived as (see Equation 11 of Tan et al. (2018))

$$\begin{aligned} \partial_t (a_p k_p) + \partial_z (a_p w_p k_p) = & -a_p \overline{w_p' \boldsymbol{u}_{h,p}'} \cdot \partial_z \boldsymbol{u}_{h,p} + a_p \overline{w_p' b_p'} \\ & + E\left(k_e + \frac{1}{2}\|\boldsymbol{u}_e - \boldsymbol{u}_p\|^2 \right) - D k_p \\ & - \partial_z \left(a_p \overline{w_p' \frac{\boldsymbol{u}_p' \cdot \boldsymbol{u}_p'}{2}} + a_p \overline{\boldsymbol{u}_p' \cdot \frac{1}{\rho_0} (\nabla p^{\dagger})_p'} \right) - a_p \epsilon_p \end{aligned} \tag{C1}$$

Consistent with the neglect of subplume fluxes and temporal tendency in EDMF (see Part I or Tan et al. (2018)), we propose as a first attempt to retain advection, entrainment, detrainment and dissipation terms, which lead to the simplified form of the previous equation:

$$\partial_z (a_p w_p k_p) = E\left(k_e + \frac{1}{2}\|\boldsymbol{u}_e - \boldsymbol{u}_p\|^2 \right) - D k_p - a_p \epsilon_p$$

Our goal is now to express $k_e + \frac{1}{2}\|\boldsymbol{u}_e - \boldsymbol{u}_p\|^2$ in terms of plume variables only. We apply the plume/environment decomposition to TKE starting from (B1), leading to

$$k_e = \frac{1}{a_e} k - \frac{1}{a_e} a_p \left(k_p + \frac{1}{2}\|\boldsymbol{u}_p - \overline{\boldsymbol{u}}\|^2 \right) - \frac{1}{2}\|\boldsymbol{u}_e - \overline{\boldsymbol{u}}\|^2 \tag{C2}$$

$$= \frac{1}{a_e} k - \frac{1}{a_e} a_p \left(k_p + \frac{1}{2}\|\boldsymbol{u}_p - \overline{\boldsymbol{u}}\|^2 \right) - \frac{1}{a_e^2} a_p^2 \frac{1}{2}\|\boldsymbol{u}_p - \overline{\boldsymbol{u}}\|^2 \tag{C3}$$

where the last equality is obtained using the identity $\boldsymbol{u}_e - \overline{\boldsymbol{u}} = -a_p/a_e(\boldsymbol{u}_p - \overline{\boldsymbol{u}})$. Then we use the identity $\boldsymbol{u}_e - \boldsymbol{u}_p = 1/a_e(\boldsymbol{u}_p - \overline{\boldsymbol{u}})$ to obtain

$$\begin{aligned} k_e + \frac{1}{2}\|\boldsymbol{u}_e - \boldsymbol{u}_p\|^2 &= \frac{1}{a_e} k - \frac{1}{a_e} a_p \left(k_p + \frac{1}{2}\|\boldsymbol{u}_p - \overline{\boldsymbol{u}}\|^2 \right) - \frac{1}{a_e^2} a_p^2 \frac{1}{2}\|\boldsymbol{u}_p - \overline{\boldsymbol{u}}\|^2 + \frac{1}{a_e^2} \frac{1}{2}\|\boldsymbol{u}_p - \overline{\boldsymbol{u}}\|^2 \\ &= \frac{1}{a_e} k - \frac{1}{a_e} a_p k_p + \frac{1}{a_e} \frac{1}{2}\|\boldsymbol{u}_p - \overline{\boldsymbol{u}}\|^2 \left(-a_p - \frac{1}{a_e} a_p^2 + \frac{1}{a_e} \right) \end{aligned} \tag{C4}$$

$$= \frac{1}{a_e} k - \frac{1}{a_e} a_p k_p + \frac{1}{a_e} \frac{1}{2}\|\boldsymbol{u}_p - \overline{\boldsymbol{u}}\|^2 \frac{-a_p(1 - a_p) - a_p^2 + 1}{a_e} \tag{C5}$$

$$= \frac{1}{a_e}k - \frac{1}{a_e}a_p k_p + \frac{1}{a_e}\frac{1}{2}\|\boldsymbol{u}_p - \overline{\boldsymbol{u}}\|^2 \underbrace{\frac{1-a_p}{a_e}}_{=1} \tag{C6}$$

and thus the plume TKE budgets rewrites as

$$\partial_z(a_p w_p k_p) = E\frac{1}{1-a_p}\left(k - a_p k_p + \frac{1}{2}\|\boldsymbol{u}_p - \overline{\boldsymbol{u}}\|^2\right) - Dk_p - a_p\epsilon_p \tag{C7}$$

Using area conservation $\partial_z(a_p w_p) = E - D$, we get the advective form

$$a_p w_p \partial_z k_p = E\frac{1}{1-a_p}\left(k - k_p + \frac{1}{2}\|\boldsymbol{u}_p - \overline{\boldsymbol{u}}\|^2\right) - a_p\epsilon_p \tag{C8}$$

Finally assuming $\frac{1}{1-a_p} \simeq 1$ (i.e., the small area limit) we have the desired expression (Equation 14).

$$a_p w_p \partial_z k_p = E\left(k - k_p + \frac{1}{2}\|\boldsymbol{u}_p - \overline{\boldsymbol{u}}\|^2\right) - a_p\epsilon_p \tag{C9}$$

Appendix D: Discretization of Mass-Flux Equations

We start from the standard grid arrangement used in oceanic models which are usually discretized on a Lorenz grid in the vertical (density is located in the center of the cells on the vertical). We consider N grid cells in the vertical with thickness $\Delta z_j = z_{j+1/2} - z_{j-1/2}$ ($z_{1/2} = -H$ and $z_{N+1/2} = 0$ the surface) such that $\sum_{j=1}^{N}\Delta z_j = -H$. For the discrete values, not to interfere with the grid indices, the subscript p for the plume quantities is now a superscript such that plume quantities are now noted $X^p_{j+1/2} = X_p(z = z_{j+1/2})$. In the following, we consider that the plume quantities and k are discretized at cell interfaces and the mean quantities $\overline{X}$ are discretized at cell centers and are interpreted in a finite-volume sense (i.e., $\overline{X}_j = \frac{1}{\Delta z_j}\int_{z_{j-1/2}}^{z_{j+1/2}}\overline{X}(z)\,\mathrm{d}z$). We start from the mass-flux equations given in Table 1 with $\tilde{b}' = b'/h$ but in conservative form (except for the vertical velocity and TKE plume equations) and assuming that a_p is small:

$$\partial_z(a_p w_p) = E - D \tag{D1}$$

$$\partial_z\left(a_p w_p \phi_p\right) = E\overline{\phi} - D\phi_p + a_p S_{\phi,p} \tag{D2}$$

$$\partial_z(a_p w_p \boldsymbol{U}_p) = E\overline{\boldsymbol{U}} - D\boldsymbol{U}_p \tag{D3}$$

$$w_p\partial_z w_p = -(E/a_p)\,(b w_p) + aB_p + \tilde{b}' w_p^2 \tag{D4}$$

$$a_p w_p \partial_z k_p = E\left(k - k_p + \frac{1}{2}(\overline{\boldsymbol{u}}_p - \overline{\boldsymbol{u}})^2\right) - a_p\epsilon_p \tag{D5}$$

where the equation for horizontal momentum has been manipulated to have the same form as the ϕ_p equation by taking $\boldsymbol{U}_p = \boldsymbol{u}_{h,p} - C_u\overline{\boldsymbol{u}}_h$ and $\overline{\boldsymbol{U}} = (1 - C_u)\,\overline{\boldsymbol{u}}_h$, and $S_{\phi,p}$ is a source term. The advective form is used for the w_p equation to make the computation of w_p independent of a_p (with the closure hypothesis given in Table 1 for E, E/a_p is independent of a_p); the motivations for this will become clearer later. The mass-flux equations correspond to a first-order nonlinear set of ODEs. There are a lot of methods for solving such initial value problems. We present here a simple method combining explicit (Euler) and semi-implicit (Crank-Nicolson) steps as the use of more advanced methods did not produce significantly different results (we tested a spline-based high-order finite-volume method as well as a non-standard finite difference method, the latter being particularly well-

suited for solving nonlinear ODEs). In the following, we describe the different steps for the resolution starting from known initial values $X^p_{N+1/2}$ at the surface and advancing downward.

D1. Surface Boundary Conditions

The discrete form of the boundary conditions given in Equation 57 are obtained by a linear extrapolation of $\overline{\phi}_N$ and $(\overline{\boldsymbol{u}}_h)_N$ toward the surface, as plume variables are defined on cell interfaces while mean variables are defined at the center of the cell (by doing this extrapolation, we implicitly assume that there is no entrainment in the top most half cell).

$$w^p_{N+1/2} = w^p_0 \tag{D6}$$

$$\phi^p_{N+1/2} = \frac{(2\Delta z_N + \Delta z_{N-1})\overline{\phi}_N - \Delta z_N \overline{\phi}_{N-1}}{\Delta z_N + \Delta z_{N-1}} \tag{D7}$$

$$\boldsymbol{U}^p_{N+1/2} = (1 - C_u)\,\frac{(2\Delta z_N + \Delta z_{N-1})\,(\overline{\boldsymbol{u}}_h)_N - \Delta z_N (\overline{\boldsymbol{u}}_h)_{N-1}}{\Delta z_N + \Delta z_{N-1}} \tag{D8}$$

where w^p_0 is a fixed minimum value for w_p. Since the TKE k is already discretized at cell interfaces the boundary condition for k_p does not require an extrapolation. In particular the condition on ϕ_p leads to the following value of the B_p term in the topmost grid cell:

$$B^p_N = \Delta z_N \left(\frac{\overline{b}_N - \overline{b}_{N-1}}{\Delta z_N + \Delta z_{N-1}}\right) = \frac{\Delta z_N}{2}\left(N^2\right)_{N-1/2} \tag{D9}$$

meaning that using the condition (Equation D7) allows to triggering convection as soon as the Brunt-Väisälä frequency $\left(N^2\right)_{N-1/2}$ is negative. Indeed, a negative value of B^p_N in the RHS of the w_p-Equation D4 leads to a positive value of $\left(\partial_z w_p\right)_N$ and thus larger negative values of w_p when going downward.

D2. w_p-Equation and Mixed Layer Depth

The w_p-Equation D4 using the entrainment E given in Table 1 can be formulated as

$$\partial_z w_p^2 + bC_{\text{ent}}\,\min\left(\partial_z w_p^2, 0\right) = 2aB_p + 2\tilde{b}' w_p^2 \tag{D10}$$

which can be discretized in a straightforward way as

$$\begin{aligned} \tilde{\beta}\left[(w^p)^2_{j+1/2} - (w^p)^2_{j-1/2}\right] &= 2a\Delta z_j B^p_j + \left(\tilde{b}'\Delta z_j\right)\left[(w^p)^2_{j+1/2} + (w^p)^2_{j-1/2}\right] \\ B^p_j &= b_{\text{eos}}\left(\phi^p_{j+1/2}\right) - b_{\text{eos}}\left(\overline{\phi}_j\right) \end{aligned} \tag{D11}$$

where $\tilde{\beta} = 1 + bC_{\text{ent}}$ if $aB^p_j + \tilde{b}'(w^p)^2_{j+1/2}$ is negative and $\tilde{\beta} = 1$ otherwise. Knowing $w^p_{j+1/2}$, it is easily found that

$$(w^p)^2_{j-1/2} = \frac{\left(\tilde{\beta} - \tilde{b}'\Delta z_j\right)(w^p)^2_{j+1/2} - 2a\Delta z_j B^p_j}{\tilde{\beta} + \tilde{b}'\Delta z_j} \tag{D12}$$

Once this quantity falls below a certain threshold $(w^p_{\min})^2$, the plume is considered evanescent. In the oceanic context we consider $w^p_{j-1/2} = -\sqrt{(w^p)^2_{j-1/2}}$ for the rest of the calculations to guarantee that $w^p_{j-1/2}$ is strictly negative. The upwinding used to compute B_p in Equation D11 in addition to the fact that the w_p-equation does not depend on a_p avoid the need for an iterative process to solve the mass-flux equations.

The MLD h we considered to scale the parameter b' is the depth at which the discrete value of w^p equals $w^p_{\min}$. In practice, as soon as $(w^p)^2_{j-1/2}$ given by Equation D12 is smaller than $(w^p_{\min})^2$ we use (Equation D12) to compute the distance $\Delta z^\star_j$ below $z_{j+1/2}$ where the plume vertical velocity exactly equals $w^p_{\min}$:

$$\Delta z^\star_j = \frac{(w^p)^2_{j+1/2} - (w^p_{\min})^2}{2aB^p_j + \tilde{b}'\left((w^p)^2_{j+1/2} + (w^p_{\min})^2\right)} \tag{D13}$$

leading to $h = z_{j+1/2} - \Delta z^\star_j$. To compute $\Delta z^\star_j$ we assume that $\tilde{\beta} = 1$ because the bottom of the plume is reached only if we are in the detrainment zone.

D3. Continuity and Tracer Equations

The entrainment E_j and detrainment D_j rates given in Table 1 (taken from Rio et al. (2010)) discretized on a grid cell j correspond to

$$\Delta z_j E_j = \frac{1}{2}(a^p_{j+1/2} + a^p_{j-1/2})\, C_{\text{ent}}\left(\delta_z w^p\right)^+_j \tag{D14}$$

$$\Delta z_j D_j = \frac{1}{2}(a^p_{j+1/2} + a^p_{j-1/2})\left[-C_{\text{det}}\left(\delta_z w^p\right)^-_j - \frac{\delta_0 \Delta z_j}{2h}(w^p_{j+1/2} + w^p_{j-1/2})\right] \tag{D15}$$

where $\left(\delta_z w^p\right)^+_j = \max(w^p_{j+1/2} - w^p_{j-1/2}, 0)$ and $\left(\delta_z w^p\right)^-_j = \min(w^p_{j+1/2} - w^p_{j-1/2}, 0)$. Integrating from $z_{j-1/2}$ to $z_{j+1/2}$ the continuity equation and ϕ_p equations we obtain

$$(a^p w^p)_{j+1/2} - (a^p w^p)_{j-1/2} = \Delta z_j (E_j - D_j) \tag{D16}$$

$$(a^p w^p \phi^p)_{j+1/2} - (a^p w^p \phi^p)_{j-1/2} = \Delta z_j E_j \overline{\phi}_j - (\Delta z_j D_j/2)\left(\phi^p_{j+1/2} + \phi^p_{j-1/2}\right) + \left(S^p_\phi\right)_j \tag{D17}$$

which can also be extended to the horizontal momentum equation formulated using $\boldsymbol{U}_p$. Since at this stage $w^p_{j+1/2}$ and $w^p_{j-1/2}$ are known, the continuity equation is used to compute $a^p_{j-1/2}$ through

$$\begin{aligned} a^p_{j-1/2} &= a^p_{j+1/2}\left\{\frac{2w^p_{j+1/2} - \text{EmD}_j}{2w^p_{j-1/2} + \text{EmD}_j}\right\} \\ \text{EmD}_j &= C_{\text{ent}}\left(\delta_z w^p\right)_j{}^+ + C_{\text{det}}\left(\delta_z w^p\right)_j{}^- + \min\left\{\frac{\delta_0 \Delta z_j}{2h}(w^p_{j+1/2} + w^p_{j-1/2}), 2w^p_{\min}\right\} \end{aligned} \tag{D18}$$

Note that a_p is subject to a boundedness requirement as $0 \le a_p \le 1$. Assuming $0 \le a^p_{j+1/2} \le 1$, sufficient conditions to guarantee that $a^p_{j-1/2} \le 1$ are $C_{\text{ent}} \le 1$ and $C_{\text{det}} \ge 1$ and a sufficient condition to guarantee that $a^p_{j-1/2} \ge 0$ is $C_{\text{det}} < 2$. Moreover, a constraint is added on the background detrainment δ_0 in Equation D18 to guarantee that $a^p_{j-1/2} = 0$ as soon as $w^p_{j+1/2} = w^p_{j-1/2} = w^p_{\min}$ which occurs once outside the plume.

Once $a^p_{j-1/2}$ is known, it is possible to compute $\phi^p_{j-1/2}$ (as well as $\boldsymbol{U}^p_{j-1/2}$). The proposed discretization ensures that the compatibility between the continuity and the tracer equations is maintained at the discrete level (i.e., we recover the continuity equation for $\phi^p_{j+1/2} = \phi^p_{j-1/2} = 1$ and $\overline{\phi}_j = 1$).

The same reasoning can be applied to solve the k_p equation, which presents no additional difficulties as all necessary quantities $w^p_{j\pm1/2}$, $a^p_{j\pm1/2}$ and $\boldsymbol{u}^p_{j\pm1/2}$ are known.

In summary, the proposed discretization guarantees that w_p is strictly negative, that a_p is bounded between 0 and 1, and that the continuity and tracer equations are compatible, without the need for an iterative solution procedure.

Appendix E: Time Step and Vertical Resolution Sensitivity

On Figure E1 we expose mixed layer depth (MLD) sensitivity to time step and vertical resolution for the case W005_C500. The vertical resolution $dz = 40$ m may seem unusually large for mixed layer simulations. However, when using a stretched grid, deep convection can reach depth at which local grid spacing on the order of 40 m, thus justifying the relevance of testing the scheme with a constant grid spacing of $dz = 40$ m.

Data Availability Statement

Idealized LES data and ASICS-MED data are available at the Zenodo archive (Lemarié & Perrot, 2025). LES data have been produced using the MESO-NH model (see next section). ASICS-MED data contain initial and boundary conditions for the SCM simulations, as well as observations of temperature and salinity profiles combined from the Hymex/ASICS-MED campaign and the Lion mooring. They were downloaded from the `ftp` server given in Giordani et al. (2020) on 1 March 2025. *Software Availability Statement* All the LES and SCM codes used in this study have been made available and can be found at the Zenodo archive (Lemarié & Perrot, 2025). The LES code consists of the 5.5.1 version of the Méso-NH model (Lac et al., 2018). The SCM model consists of low-level code written in Fortran interfaced with Python using F2PY (Peterson, 2009). The single-column simulations analyzed in this study can be executed from a high-level Python driver code without any intervention on the Fortran code. The high-level Python driver code and scripts to reproduce the figures are available in the Zenodo archive.

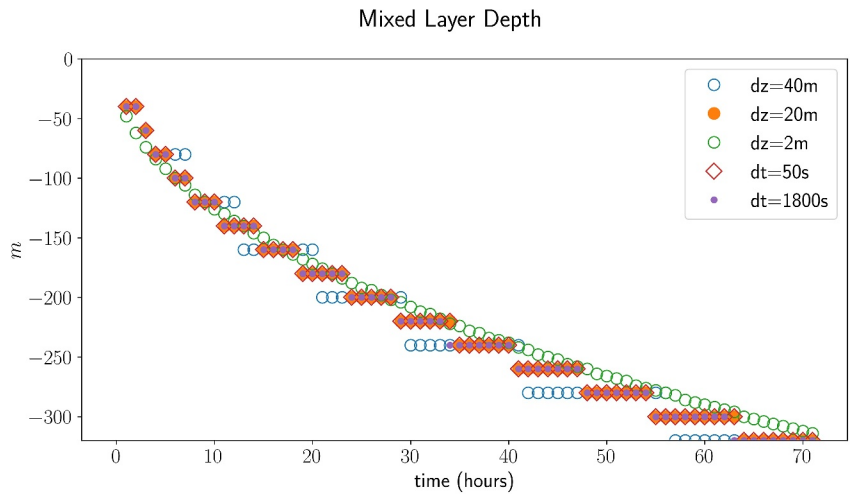

Figure E1. Mixed layer depth (MLD) computed as the minimum of temperature flux for different time steps (dt) and vertical resolutions (dz), Large Eddy Simulations data and analytical expression.

Acknowledgments
The authors would like to thank Hilary Weller and two anonymous reviewers for their thoughtful reading and constructive comments that greatly helped improving the manuscript. This work was supported by the *institut des Mathématiques pour la Planète Terre* (iMPT) through the project "Coherent sub-grid scale modeling for ocean climate models." This study was carried out as part of the technological defense project PROTEVS2 under the auspices of the French Ministry of the Armies/DGA, was funded in part by l'Agence Nationale de la Recherche (ANR), projects ANR-23-CE01-0009 and ANR-23-CE56-0006. MP was supported by a PhD fellowship from Ecole Normale Supérieure Paris. The authors are extremely grateful to Jean-Luc Redelsperger for his essential contributions to the MESO-NH model, and to Hervé Giordani for his commitment in the creation of the ASICS-MED data set.

References

Bretherton, C. S., & Park, S. (2009). A new moist turbulence parameterization in the community atmosphere model. *Journal of Climate*, *22*(12), 3422–3448. https://doi.org/10.1175/2008JCLI2556.1

Burchard, H. (2002). Energy-conserving discretisation of turbulent shear and buoyancy production. *Ocean Modelling*, *4*(3–4), 347–361. https://doi.org/10.1016/S1463-5003(02)00009-4

Caniaux, G., Prieur, L., Giordani, H., & Redelsperger, J.-L. (2017). An inverse method to derive surface fluxes from the closure of oceanic heat and water budgets: Application to the north-western Mediterranean Sea. *Journal of Geophysical Research: Oceans*, *122*(4), 2884–2908. https://doi.org/10.1002/2016JC012167

Cohen, Y., Lopez-Gomez, I., Jaruga, A., He, J., Kaul, C. M., & Schneider, T. (2020). Unified entrainment and detrainment closures for extended eddy-diffusivity mass-flux schemes. *Journal of Advances in Modeling Earth Systems*, *12*(9). https://doi.org/10.1029/2020MS002162

Coppola, L., Prieur, L., Taupier-Letage, I., Estournel, C., Testor, P., Lefevre, D., et al. (2017). Observation of oxygen ventilation into deep waters through targeted deployment of multiple argo-o2 floats in the north-western mediterranean sea in 2013. *Journal of Geophysical Research*, *122*(8), 6325–6341. https://doi.org/10.1002/2016JC012594

Couvreux, F., Hourdin, F., & Rio, C. (2010). Resolved versus parametrized boundary-layer plumes. Part I: A parametrization-oriented conditional sampling in large-eddy simulations. *Boundary-Layer Meteorology*, *134*(3), 441–458. https://doi.org/10.1007/s10546-009-9456-5

Couvreux, F., Hourdin, F., Williamson, D., Roehrig, R., Volodina, V., Villefranque, N., et al. (2021). Process-based climate model development harnessing machine learning: I. A calibration tool for parameterization improvement. *Journal of Advances in Modeling Earth Systems*, *13*(3), e2020MS002217. https://doi.org/10.1029/2020MS002217

Cuxart, J., Bougeault, P., & Redelsperger, J.-L. (2000). A turbulence scheme allowing for mesoscale and large-eddy simulations. *Quarterly Journal of the Royal Meteorological Society*, *126*(562), 1–30. https://doi.org/10.1002/qj.49712656202

Deardorff, J. W. (1970). Convective velocity and temperature scales for the unstable planetary boundary layer and for Rayleigh convection. *Journal of the Atmospheric Sciences*, *27*(8), 1211–1213. https://doi.org/10.1175/1520-0469(1970)027⟨1211:CVATSF⟩2.0.CO;2

Dunbar, O. R. A., Garbuno-Inigo, A., Schneider, T., & Stuart, A. M. (2021). Calibration and uncertainty quantification of convective parameters in an idealized GCM. *Journal of Advances in Modeling Earth Systems*, *13*(9). https://doi.org/10.1029/2020MS002454

Estournel, C., Testor, P., Taupier-Letage, I., Bouin, M.-N., Coppola, L., Durand, P., et al. (2016). Hymex-sop2: The field campaign dedicated to dense water formation in the northwestern mediterranean. *Oceanography*, *29*(4), 196–206. https://doi.org/10.5670/oceanog.2016.94

Garanaik, A., Pereira, F. S., Smith, K., Robey, R., Li, Q., Pearson, B., & Van Roekel, L. (2024). A new hybrid mass-flux/high-order turbulence closure for ocean vertical mixing. *Journal of Advances in Modeling Earth Systems*, *16*(1). https://doi.org/10.1029/2023MS003846

Garcia, J. R., & Mellado, J. P. (2014). The two-layer structure of the entrainment zone in the convective boundary layer. *Journal of the Atmospheric Sciences*, *71*(6), 1935–1955. https://doi.org/10.1175/JAS-D-13-0148.1

Garratt, J. (1994). *The atmospheric boundary layer*. Cambridge University Press.

Gaspar, P., Grégoris, Y., & Lefevre, J.-M. (1990). A simple eddy kinetic energy model for simulations of the oceanic vertical mixing: Tests at station Papa and long-term upper ocean study site. *Journal of Geophysical Research*, *95*(C9), 16179–16193. https://doi.org/10.1029/JC095iC09p16179

Giordani, H., Bourdallé-Badie, R., & Madec, G. (2020). An eddy-diffusivity mass-flux parameterization for modeling oceanic convection. *Journal of Advances in Modeling Earth Systems*, *12*(9). https://doi.org/10.1029/2020MS002078

Greenhut, G. K., & Khalsa, S. J. S. (1982). Updraft and downdraft events in the atmospheric boundary layer over the equatorial Pacific ocean. *Journal of the Atmospheric Sciences*, *39*(8), 1803–1818. https://doi.org/10.1175/1520-0469(1982)039⟨1803:UADEIT⟩2.0.CO;2

Haghshenas, A., & Mellado, J. P. (2019). Characterization of wind-shear effects on entrainment in a convective boundary layer. *Journal of Fluid Mechanics*, *858*, 145–183. https://doi.org/10.1017/jfm.2018.761

Han, J., & Bretherton, C. S. (2019). TKE-based moist eddy-diffusivity mass-flux (EDMF) parameterization for vertical turbulent mixing. *Weather and Forecasting*, *34*(4), 869–886. https://doi.org/10.1175/WAF-D-18-0146.1

Honnert, R. (2022). De la zone grise de la turbulence à AROME hectométrique (thesis, Université Toulouse 3 Paul Sabatier). Retrieved from https://hal.science/tel-03600147

Houpert, L., Durrieu de Madron, X., Testor, P., Bosse, A., D'Ortenzio, F., Bouin, M. N., et al. (2016). Observations of open-ocean deep convection in the northwestern Mediterranean Sea: Seasonal and interannual variability of mixing and deep water masses for the 2007-2013 period. *Journal of Geophysical Research*, *121*(11), 8139–8171. https://doi.org/10.1002/2016JC011857

Hourdin, F., Mauritsen, T., Gettelman, A., Golaz, J.-C., Balaji, V., Duan, Q., et al. (2017). The art and science of climate model tuning. *Bulletin America Meteorology Social*, *98*(3), 589–602. https://doi.org/10.1175/BAMS-D-15-00135.1

Lac, C., Chaboureau, J.-P., Masson, V., Pinty, J.-P., Tulet, P., Escobar, J., et al. (2018). Overview of the Meso-NH model version 5.4 and its applications. *Geoscientific Model Development*, *11*(5), 1929–1969. https://doi.org/10.5194/gmd-11-1929-2018

Legay, A., Deremble, B., Penduff, T., Brasseur, P., & Molines, J.-M. (2024). A framework for assessing ocean mixed layer depth evolution. *Journal of Advances in Modeling Earth Systems*, *16*(10), e2023MS004198. https://doi.org/10.1029/2023MS004198

Lemarié, F., & Perrot, M. (2025). Data and code for "energetically consistent eddy-diffusivity mass-flux convective schemes. part II: Implementation and evaluation in an oceanic context". https://doi.org/10.5281/zenodo.15593855

Madec, G., Bourdallé-Badie, R., Chanut, J., Clementi, E., Coward, A., Ethé, C., et al. (2019). NEMO ocean engine. https://doi.org/10.5281/ZENODO.1464816

Marshall, J., & Schott, F. (1999). Open-ocean convection: Observations, theory, and models. *Reviews of Geophysics*, *37*(1), 1–64. https://doi.org/10.1029/98RG02739

McDougall, T. J. (2003). Potential enthalpy: A conservative oceanic variable for evaluating heat content and heat fluxes. *Journal of Physical Oceanography*, *33*(5), 945–963. https://doi.org/10.1175/1520-0485(2003)033⟨0945:PEACOV⟩2.0.CO;2

Mellor, G. (1973). Analytic prediction of the properties of stratified planetary surface layers. *Journal of the Atmospheric Sciences*, *30*(6), 1061–1069. https://doi.org/10.1175/1520-0469(1973)030⟨1061:APOTPO⟩2.0.CO;2

Obukhov, A. M. (1971). Turbulence in an atmosphere with a non-uniform temperature. *Bound.-Lay. Meteorol*, *2*(1), 7–29. https://doi.org/10.1007/BF00718085

Park, S.-B., Gentine, P., Schneider, K., & Farge, M. (2016). Coherent structures in the boundary and cloud layers: Role of updrafts, subsiding shells, and environmental subsidence. *Journal of the Atmospheric Sciences*, *73*(4), 1789–1814. https://doi.org/10.1175/JAS-D-15-0240.1

Pergaud, J., Masson, V., Malardel, S., & Couvreux, F. (2009). A parameterization of dry thermals and shallow cumuli for mesoscale numerical weather prediction. *Boundary-Layer Meteorology*, *132*(1), 83–106. https://doi.org/10.1007/s10546-009-9388-0

Perrot, M., Lemarié, F., & Dubos, T. (2025). Energetically consistent eddy-diffusivity mass-flux convective schemes: 1. Theory and models. *Journal of Advances in Modeling Earth Systems*, *17*(1), e2024MS004273. https://doi.org/10.1029/2024ms004273

Peterson, P. (2009). F2PY: A tool for connecting fortran and Python programs. *International Journal of Computer Science and Engineering*, *4*(4), 296. https://doi.org/10.1504/IJCSE.2009.029165

Pope, S. B. (2004). Ten questions concerning the large-eddy simulation of turbulent flows. *New Journal of Physics*, *6*, 35. https://doi.org/10.1088/1367-2630/6/1/035

Ramadhan, A., Wagner, G. L., Hill, C., Campin, J.-M., Churavy, V., Besard, T., et al. (2020). Oceananigans.jl: Fast and friendly geophysical fluid dynamics on GPUs. *Journal of Open Source Software*, *5*(53), 2018. https://doi.org/10.21105/joss.02018

Rio, C., Hourdin, F., Couvreux, F., & Jam, A. (2010). Resolved versus parametrized boundary-layer plumes. Part II: Continuous formulations of mixing rates for mass-flux schemes. *Boundary-Layer Meteorology*, *135*(3), 469–483. https://doi.org/10.1007/s10546-010-9478-z

Siebesma, A. P., Soares, P. M. M., & Teixeira, J. (2007). A combined eddy-diffusivity mass-flux approach for the convective boundary layer. *Journal of the Atmospheric Sciences*, *64*(4), 1230–1248. https://doi.org/10.1175/JAS3888.1

Soares, P. M. M., Miranda, P. M. A., Siebesma, A. P., & Teixeira, J. (2004). An eddy-diffusivity/mass-flux parametrization for dry and shallow cumulus convection. *Quarterly Journal of the Royal Meteorological Society*, *130*(604), 3365–3383. https://doi.org/10.1256/qj.03.223

Souza, A. N., Wagner, G. L., Ramadhan, A., Allen, B., Churavy, V., Schloss, J., et al. (2020). Uncertainty quantification of ocean parameterizations: Application to the K-Profile-Parameterization for penetrative convection. *Journal of Advances in Modeling Earth Systems*, *12*(12). https://doi.org/10.1029/2020MS002108

Suselj, K., Kurowski, M. J., & Teixeira, J. (2019). A unified eddy-diffusivity/mass-flux approach for modeling atmospheric convection. *Journal of the Atmospheric Sciences*, *76*(8), 2505–2537. https://doi.org/10.1175/JAS-D-18-0239.1

Tailleux, R., & Dubos, T. (2024). A simple and transparent method for improving the energetics and thermodynamics of seawater approximations: Static energy asymptotics (SEA). *Ocean Modelling*, *188*, 102339. https://doi.org/10.1016/j.ocemod.2024.102339

Tan, Z., Kaul, C. M., Pressel, K. G., Cohen, Y., Schneider, T., & Teixeira, J. (2018). An extended eddy-diffusivity mass-flux scheme for unified representation of subgrid-scale turbulence and convection. *Journal of Advances in Modeling Earth Systems*, *10*(3), 770–800. https://doi.org/10.1002/2017MS001162

Turner, J. S. (1979). *Buoyancy effects in fluids*. Cambridge University Press.

Van Roekel, L., Adcroft, A. J., Danabasoglu, G., Griffies, S. M., Kauffman, B., Large, W., et al. (2018). The KPP boundary layer scheme for the Ocean: Revisiting its formulation and Benchmarking one-dimensional simulations relative to LES. *Journal of Advances in Modeling Earth Systems*, *10*(11), 2647–2685. https://doi.org/10.1029/2018MS001336

Waldman, R., Somot, S., Herrmann, M., Bosse, A., Caniaux, G., Estournel, C., et al. (2017). Modeling the intense 2012-2013 dense water formation event in the northwestern Mediterranean Sea: Evaluation with an ensemble simulation approach. *Journal of Geophysical Research*, *122*(2), 1297–1324. https://doi.org/10.1002/2016JC012437

Witek, M. L., Teixeira, J., & Matheou, G. (2011). An eddy diffusivity–mass flux approach to the vertical transport of turbulent kinetic energy in convective boundary layers. *Journal of the Atmospheric Sciences*, *68*(10), 2385–2394. https://doi.org/10.1175/JAS-D-11-06.1

Yano, J.-I. (2014). Formulation structure of the mass-flux convection parameterization. *Dynamics of Atmospheres and Oceans*, *67*, 1–28. https://doi.org/10.1016/j.dynatmoce.2014.04.002

Zheng, Z., Harcourt, R. R., & D'Asaro, E. A. (2021). Evaluating Monin–Obukhov scaling in the unstable oceanic surface layer. *Journal of Physical Oceanography*, *51*(3), 911–930. https://doi.org/10.1175/JPO-D-20-0201.1

Zhou, B., Sun, S., Yao, K., & Zhu, K. (2018). Reexamining the gradient and Countergradient representation of the local and Nonlocal heat fluxes in the convective boundary layer. *Journal of the Atmospheric Sciences*, *75*(7), 2317–2336. https://doi.org/10.1175/JAS-D-17-0198.1